A coarse-grained decomposition of surface geostrophic kinetic energy in the global ocean

M. Buzzicotti[1], B. A. Storer[2], S.M. Griffies[3,4], and H. Aluie[2,5]

[1]1Department of Physics, University of Rome Tor Vergata and INFN
[2]Department of Mechanical Engineering, University of Rochester
[3]NOAA Geophysical Fluid Dynamics Laboratory
[4]Princeton University Atmospheric and Oceanic Sciences Program
[5]Laboratory for Laser Energetics University of Rochester

Key Points:

- Coarse-graining decomposes ocean geostrophic kinetic energy according to length-scale and reveals a spring peak.
- Reynolds averaging provides an imprecise decomposition of energy according to length-scale.
- AVISO gridded product suppresses temporal variations less than 10 days, especially between 100 km and 500 km.

Corresponding author: Hussein Aluie, `hussein@rochester.edu`

Abstract

We apply a coarse-grained decomposition of the ocean's surface geostrophic flow derived from satellite and numerical model products. In the extra-tropics we find that roughly 60% of the global surface geostrophic kinetic energy is at scales between 100 km and 500 km, peaking at ≈ 300 km. Our analysis also reveals a clear seasonality in the kinetic energy with a spring peak. We show that traditional mean-fluctuation (or Reynolds) decomposition is unable to robustly disentangle length-scales since the time mean flow consists of a significant contribution (greater than 50%) from scales < 500 km. By coarse-graining in both space and time, we find that every length-scale evolves over a wide range of time-scales. Consequently, a running time-average of any duration reduces the energy content of all length-scales, including those larger than 1000 km, and is not effective at removing length-scales smaller than 300 km. By contrasting our spatio-temporal analysis of numerical model and satellite products, we show that the AVISO gridded product suppresses temporal variations less than 10 days for *all length-scales*, especially between 100 km and 500 km.

Plain Language Summary

Traditionally, 'eddies' are identified as transient features that vary in time relative to a background time mean flow. As such, a 'mean' flow does not necessarily imply a large length-scale flow. For example, standing eddies or stationary meanders due to topographic interactions have little variation in time, but can still have significant energy at small length scales. Similarly, 'eddy', 'time-varying' or 'transient' do not necessarily imply small length-scale, with examples including the large-scale transient motions from Rossby waves or fluctuations of the Kuroshio Current. Hence, the traditional time average approach offers no control over the specific physical length that divides oceanic flow into 'large' and 'small'. That is, the length-scales constituting the large-scale flow cannot be varied/controlled by time averaging in a manner that is consistent with length-scales resolved in a coarse climate simulation.

We consider a coarse-graining method to studying geostrophic ocean currents with this method consistent with our notions of 'mesoscale' as defined by a length scale. Our approach is directly relevant to scale-aware parameterization requirements of coarse-resolution simulations, since we are directly focused on length-scales of the flow fields. To illustrate the coarse-graining method, and to add understanding to the oceanic flows analyzed here, we present the first global characterization of kinetic energy content and its temporal variation as decomposed by coarse-graining according to precisely defined length-scales.

1 Introduction

The oceanic circulation emerges from a suite of linear and nonlinear dynamical processes that act over a broad range of space and time scales. The flow field is markedly inhomogeneous and characterized by waves, instabilities, and turbulent eddies, each of which are subject to a variety of energetic sources and sinks. The mesoscale defines a key band of spatial scales where ocean flows are largely geostrophic and where kinetic energy peaks (Wunsch, 2007). Correspondingly, it is widely recognized that flow at the ocean mesoscales, and its response to changes in atmospheric forcing, are fundamental to the large-scale circulation and central for regional and global transport of heat and biogeochemical tracers (Ferrari & Wunsch, 2009).

However, significant gaps remain in our understanding of the mesoscale flows and their role in ocean circulation and climate. In particular, from a numerical modeling perspective, despite the ever-increasing ability to conduct simulations with mesoscale eddy-rich general circulation models (GCMs), accurately resolving these scales in routine climate-

scale (order centuries and longer) simulations remains prohibitively expensive; e.g., (Griffies et al., 2015). We are thus confronted with the need for mesoscale eddy parameterizations for the foreseeable future (Pearson et al., 2017).

A central question of physical oceanography, and in particular the eddy parameterization problem, concerns a characterization of flow features according to length-scale. This question motivates the goal of this paper, which is to provide a length-scale decomposition of the global ocean geostrophic kinetic energy, and to study the seasonal variations of this decomposition. This goal has previously been unavailable due to limitations of the commonly used Fourier spectral methods, which are unsuited to global ocean analysis due to the complex geometry of ocean basins. We thus make use of a coarse-graining method that does not share the limitations of Fourier analysis. This paper thus serves to detail the use of coarse-graining for the purpose of decomposing ocean kinetic energy, and in so doing we uncover some rather novel features of the ocean surface circulation as a function of length scale.

1.1 Limitations of Fourier methods for the ocean

It is common to quantify the spectral distribution of ocean kinetic energy via Fourier transforms computed either along transects or within regions; e.g., Fu and Smith (1996); Chen et al. (2015); Rocha et al. (2016); Khatri et al. (2018); O'Rourke et al. (2018); Callies and Wu (2019). This approach has rendered great insights into the length scales of oceanic motion and the cascade of energy through these scales (Scott & Wang, 2005; Scott & Arbic, 2007; Arbic et al., 2012, 2013, 2014). However, it has notable limitations for the ocean where the spatial domain is generally not periodic, thus necessitating adjustments to the data (e.g., by tapering) before applying Fourier transforms. Methods to produce an artifically periodic dataset can introduce spurious gradients, length-scales, and flow features not present in the original data (Sadek & Aluie, 2018). A related limitation concerns the chosen region size, with this size introducing an artificial upper length scale cutoff. In this manner, no scales are included that are larger than the region size even if larger structures exist in the ocean. Furthermore, the data is typically assumed to lie on a flat tangent plane to enable the use of Cartesian coordinates. However, if the region becomes large enough to sample the earth's curvature, then that puts into question the use of the familiar Cartesian Fourier analysis of sines and cosines. The use of spherical harmonics, common for the atmosphere, is not suitable for the ocean, again since the ocean boundaries are complex. These limitations mean that in practice, Fourier methods are only suited for open ocean regions away from boundaries, and over a rather limited regional size.

1.2 Eddy and mean flow decomposition using time averages

A traditional approach to extract the "eddies" from a flow uses time averaging. This approach is relatively simple operationally and it accords with the common practice in atmospheric and oceanic sciences of studying long-term climate means and fluctuations relative to that mean. As part of this decomposition for turbulent flow, we typically utilize the time averaging operator as a Reynolds averaging (RA) operator, whereby the average of a fluctuating quantity vanishes (Vallis, 2017). This assumption is largely based on practical considerations, with Reynolds averages strictly holding only for ensemble averages that are unavailable for most applications.

However, within the traditional decomposition, 'time mean' flow does not necessarily imply a large length-scale flow as we shall discuss in this paper. For example, standing eddies or stationary meanders due to topography (Youngs et al., 2017) have little temporal fluctuations but can have much structure at length-scales $\mathcal{O}(100)$km or smaller. Similarly, with a temporal decomposition, 'eddy' does not necessarily imply small length-scale. For example, a time averaging based decomposition would ascribe eddying mo-

tion to large-scale Rossby waves (Kessler, 1990) or variations in the Kuroshio Current's path (Kawabe, 1995).

Moreover, by construction, an eddy-mean decomposition limits our ability to analyze temporal variability (from intra-annual to inter-annual, (Bryan et al., 2014; Griffies et al., 2015)) of the multiscale coupling and evolution of different length-scales, including those that need to be resolved/predicted in global climate (coarse-grid) models. Therefore, it offers limited guidance for coarse-resolution models and no control over the specific physical length which partitions oceanic flow into 'large' and 'small.' In other words, the set of length-scales constituting the large-scale flow cannot be varied/controlled to be consistent with those length-scales resolved in a coarse climate simulation. In this sense, the traditional decomposition cannot help with current efforts to develop 'scale-aware' parameterizations (Ringler et al., 2013; Zanna et al., 2017; Pearson et al., 2017; Jansen et al., 2019).

1.3 Coarse-graining

In order to understand the multiscale nature of oceanic flows, while simultaneously resolving them in space and in time, we use a "coarse-graining" framework that is relatively new in large-scale physical oceanography (Aluie et al., 2018; Busecke & Abernathey, 2019; Srinivasan et al., 2019; Schubert et al., 2020; Rai et al., 2021; Barkan et al., 2021). It is a very general approach to analyzing complex flows, with rigorous foundations initially developed to model (Germano, 1992; Meneveau, 1994) and analyze (Eyink, 1995, 2005) turbulence. Aluie (2017) provides a theoretical discussion of coarse-graining and its connection to other methods in physics. The approach has been recently generalized to account for the spherical geometry of flow on Earth (Aluie, 2019), and applied to study the nonlinear cascade in the North Atlantic from an eddying simulation (Aluie et al., 2018).

The coarse-graining framework is very useful from the standpoint of ocean subgrid scale parameterizations (Fox-Kemper et al., 2011; Zanna et al., 2017; Khani et al., 2019; Jansen et al., 2019; Haigh et al., 2020; Stanley et al., 2020; Grooms et al., 2021). Namely, it provides a theoretical basis for constructing subgrid closures that faithfully reflect the dynamics at unresolved scales. A primary objective in ocean modeling is practical: an accurate subgrid parameterization that is numerically stable. Significant advances have been achieved in this regard in the fluid dynamics and turbulence community (Piomelli et al., 1991; Buzzicotti et al., 2018; Linkmann et al., 2018), and the field of large-eddy simulation (LES) is well-established (Meneveau & Katz, 2000).

Our use of coarse-graining supports the needs of parameterization, but our primary objective is to characterize the fundamental dynamics of the flow at *all* length scales. Even within the wider fluid dynamics community, much less work has been done in this regard, i.e. using coarse-graining as a "probe" of the fundamental scale-physics. For example, LES sub-grid parameterization studies are seldom concerned with using coarse-graining to probe the energy pathways across the entire range of scales, such as the cascade (Eyink, 1995; Eyink & Aluie, 2009; Kelley & Ouellette, 2011; Aluie et al., 2012; Rivera et al., 2014; Buzzicotti et al., 2018), forcing (Aluie, 2013; Rai et al., 2021), dissipation (Zhao & Aluie, 2018), or the range of coupling between different scales (Eyink, 2005; Aluie & Eyink, 2009).

As an important case in point, despite LES being a well established field in fluid dynamics since the seminal works of Leonard (1974) and Germano (1992), the idea of using coarse-graining in physical space to extract the energy content at different scales; i.e., the spectrum, was only recently established and demonstrated by Sadek and Aluie (2018). This method is central to our calculation here of the spectrum for the oceanic general circulation. A main advantage of coarse-graining is that it allows us to decompose different length scales in a flow, at any geographic location and any instant of time, without relying on assumptions of homogeneity, isotropy or domain periodicity. This gen-

erality makes it ideally suited for studying oceanic flows with complex continental boundaries over the entire globe or in any particular regions of interest and at any time.

1.4 Key results and outline of this paper

In this paper we make use of the coarse-graining method on a satellite sea surface product and a global ocean simulation. To directly compare the two products, we focus on geostrophic components to the horizontal surface velocity as diagnosed from sea level. We here highlight the key novel results from this analysis. First, we show that $\approx 60\%$ of the extra-tropical surface geostrophic kinetic energy, as estimated by satellite sea surface observations and a global ocean simulation, resides at scales between 100 km and 500 km, peaking at $\approx$ 300 km. We also show that these scales exhibit a clear seasonality, with kinetic energy peaking in spring. Furthermore, we demonstrate how coarse-graining allows us a new way to compare observations with models. In particular, comparing data from a numerical simulation with gridded satellite observations reveals that the satellite analysis misrepresents the evolution of *all length-scales* over time-scales less than ≈ 10 days, with the mis-representation being more pronounced at scales $\lesssim 500$ km. We show that this misrepresentation is due to the temporal averaging required to construct the gridded satellite product.

The paper is organized as follows. In Section 2 we give details on the coarse-graining and the Reynolds averaging methods used in this work. In Section 3 we present the data products used in our analysis. In Section 4 we discuss the main results from this analysis, following the coarse-graining decomposition such as the measurement of the energy spectrum, and the comparison with the traditional Reynolds average decomposition. At the end of Section 4 we introduce the combined spatio-temporal decomposition and compare satellite and numerical model data. In Section 5 we present our conclusions. Appendix A discusses some technical choices used when coarse-graining.

2 Coarse-graining for the ocean

In this section, we discuss the coarse-graining framework and how it is used to partition energy across length scales. We also discuss the traditional approach of temporal-based Reynolds averaging, in which the flow is decomposed into a mean and fluctuating components.

2.1 Basics of coarse-graining on the sphere

For any scalar field, $F(\mathbf{x})$, we can calculate its coarse-grained (or low-pass filtered) version, $\overline{F}_\ell(\mathbf{x})$, by convolving $F(\mathbf{x})$ with a normalized filter kernel $G_\ell(\mathbf{r})$,

$$\overline{F}_\ell(\mathbf{x}) = G_\ell * F(\mathbf{x}) \tag{1}$$

where $*$, in the context of this work, is convolution on the sphere (Aluie, 2019), $\mathbf{x}$ is geographic location on the globe, and the kernel $G_\ell(\mathbf{x})$ can be any non-negative function that is spatially localized (*i.e.* it goes to zero fairly rapidly as $\mathbf{x} \to \pm\infty$). The parameter ℓ is a length-scale related to the kernel's "width." We use the notation $\overline{(\cdots)}_\ell$ to denote a coarse-grained field. The kernel is area normalized for all ℓ, so that

$$\int G_\ell(\mathbf{x})\, \mathrm{d}\mathcal{S} = 1, \tag{2}$$

where $\mathrm{d}\mathcal{S}$ is the area element on the sphere. Correspondingly, the convolution (1) may be interpreted as an average of the function F within a region of diameter ℓ centered at location $\mathbf{x}$. By construction, at each point in space, $\mathbf{x}$, the coarse-grained field, $\overline{F}_\ell(\mathbf{x})$, contains information about the scale ℓ.

The above formalism holds for coarse-graining scalar fields. To coarse-grain a vector field on a sphere generally requires more work (Aluie, 2019). However, since we are concerned only with the surface geostrophic velocity, $\mathbf{u}(\mathbf{x}, t)$, in this work, it greatly simplifies our analysis. We assume the geostrophic velocity is non-divergent on the two-dimensional spherical surface, so that it is related to the geostrophic streamfunction ψ via

$$\mathbf{u} = \hat{\boldsymbol{e}}_r \times \nabla\psi, \tag{3}$$

with $\hat{\boldsymbol{e}}_r$ the radial unit vector in spherical coordinates, $\psi = \eta\, g/f$, η the free sea surface height (SSH), and the Coriolis parameter, $f = 2\Omega \sin(\phi)$, is a function of latitude ϕ, where Ω is Earth's spin rate.

Aluie (2019) showed that for non-divergent vector fields such as in eq. (3), coarse-graining $\mathbf{u}$ is equivalent to coarse-graining each of its Cartesian components. We therefore transform the vector from spherical (u_r, u_λ, u_ϕ) to planetary Cartesian coordinates (u_x, u_y, u_z) via:

$$\begin{aligned} u_x &= u_r \cos(\lambda)\cos(\phi) - u_\lambda \sin(\lambda) - u_\phi \cos(\lambda)\sin(\phi) \\ u_y &= u_r \sin(\lambda)\cos(\phi) + u_\lambda \cos(\lambda) - u_\phi \sin(\lambda)\sin(\phi) \\ u_z &= u_r \sin(\phi) + u_\phi \cos(\phi) \end{aligned} \tag{4}$$

where λ, ϕ are longitude and latitude, respectively, and u_λ, u_ϕ are the zonal and meridional velocity components, respectively. The radial velocity component, $u_r = 0$ for the geostrophic flow. We apply the spherical convolution operation in eq. (1) to each of u_x, u_y, u_z as scalar fields to obtain the corresponding coarse-grained fields $\overline{u_x}$, $\overline{u_y}$, $\overline{u_z}$, then retrieve the coarse-grained velocity, $\overline{\mathbf{u}}_\ell$ in spherical coordinates via

$$\begin{aligned} \text{coarse-grained radial flow} &= \overline{u_x}\cos(\lambda)\cos(\phi) + \overline{u_y}\sin(\lambda)\cos(\phi) + \overline{u_z}\sin(\phi) = 0 \\ \text{coarse-grained zonal flow} &= -\overline{u_x}\sin(\lambda) + \overline{u_y}\cos(\lambda) \\ \text{coarse-grained meridional flow} &= -\overline{u_x}\cos(\lambda)\sin(\phi) - \overline{u_y}\sin(\lambda)\sin(\phi) + \overline{u_z}\cos(\phi) \end{aligned} \tag{5}$$

That the 'coarse-grained radial flow' (i.e. vertical flow, parallel to gravity) vanishes is not obvious and was proved in Aluie (2019) and demonstrated numerically in Teeraratkul and Aluie (2021).

We emphasize that the coarse-graining algorithm we just described is valid only for non-divergent vectors such as $\mathbf{u}$ in eq. (3). Significant errors can arise for a general flow field (Teeraratkul & Aluie, 2021), where the complete coarse-graining formalism of Aluie (2019) is necessary (e.g. Aluie et al. (2018)).

We use the following coarse-graining kernel

$$G_\ell(\mathbf{x}) = \frac{A}{2}\left(1 - \tanh\left(10\left(\frac{\gamma(\mathbf{x})}{\ell/2} - 1\right)\right)\right), \tag{6}$$

as shown in Figure 1. It is essentially a top-hat kernel (Pope, 2001) but with graded edges to avoid numerical artifacts from the non-uniform discrete grid on the sphere. We use geodesic distance, $\gamma(\mathbf{x})$, between any location $\mathbf{x} = (\lambda, \phi)$ on Earth's surface relative to location (λ_0, ϕ_0) where coarse-graining is being performed, which we calculate using

$$\gamma(\mathbf{x}) = R_{\text{Earth}} \arccos\Big[\sin(\phi)\sin(\phi_0) + \cos(\phi)\cos(\phi_0)\cos(\lambda - \lambda_0)\Big]. \tag{7}$$

with $R_{\text{Earth}} = 6371$ km for Earth's radius. In eq. (6), A is a normalization factor, evaluated numerically, to ensure G_ℓ area integrates to unity as per equation (2). In general, we are not restricted to this choice of kernel; however, we use it because of its well-defined characteristic width ℓ. Indeed, a convolution with G_ℓ in equation (6) is a spatial analogue to an ℓ-day running time-average.

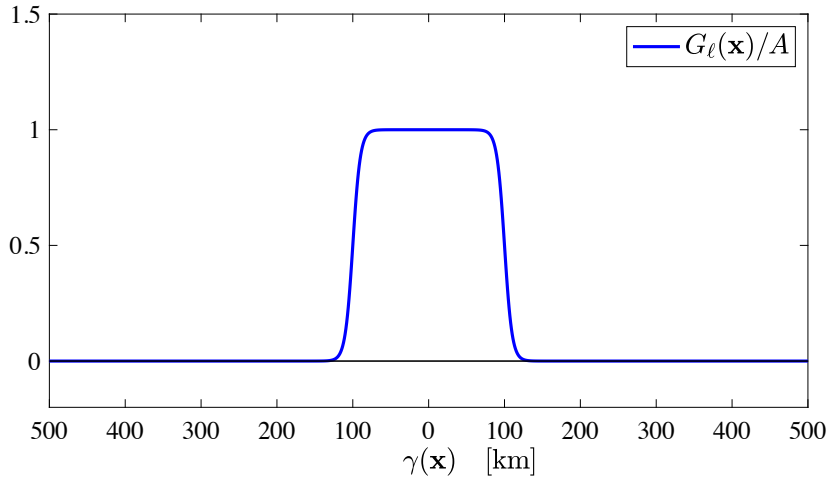

Figure 1. The coarse-graining kernel from equation (6), which is essentially a top-hat kernel (or moving window) along with graded edges to avoid numerical artifacts from the non-uniform discrete grid on the sphere. Geodesic distance $\gamma(\mathbf{x})$ is relative to location $\mathbf{x}_0$ where coarse-graining is being applied. This plot is for the un-normalized kernel, $\frac{1}{A}G_\ell(\mathbf{x})$, with $\ell = 200$ km. It is a spatial analogue for an ℓ-day window for a running time-average.

2.2 Partitioning the geostrophic kinetic energy

From the coarse-grained horizontal geostrophic velocity field, $\overline{\mathbf{u}}_\ell(\mathbf{x},t)$, following equation (1) as prescribed in (Aluie, 2019), we partition kinetic energy (KE) into different sets of length-scales:

$$\mathcal{E} = \frac{1}{2}|\mathbf{u}(\mathbf{x},t)|^2 \qquad \text{(bare KE)} \tag{8}$$

$$\mathcal{E}_\ell = \frac{1}{2}|\overline{\mathbf{u}}_\ell(\mathbf{x},t)|^2 \qquad \text{(coarse KE)} \tag{9}$$

$$\mathcal{E}_{<\ell} = \frac{1}{2}\left(\overline{|\mathbf{u}(\mathbf{x},t)|^2_\ell} - |\overline{\mathbf{u}}_\ell(\mathbf{x},t)|^2\right) \qquad \text{(fine KE).} \tag{10}$$

The "bare KE" in equation (8) is the KE per unit mass ($\mathrm{m}^2/\mathrm{s}^2$) of the original geostrophic flow that includes all scales; "coarse KE" in equation (9) represents energy of the coarse-grained geostrophic flow at length-scales larger than ℓ; and "fine KE" in equation (10) accounts for geostrophic energy at scales smaller than ℓ, which we discuss more in the following two paragraphs. Partitioning geostrophic energy across scales is not trivial since one needs to ensure that such quantities are physically valid in the sense described by Germano (1992) and Vreman et al. (1994). In particular, it is important to ensure that the partitioned kinetic energy is (i) positive semi-definite (≥ 0) at every $\mathbf{x}$ and every time, and (ii) that summing the partitions yields the total energy.

While it is clear that $\mathcal{E}_\ell \geq 0$ in equation (9), this property is not obvious for $\mathcal{E}_{<\ell}$ in equation (10). Moreover, it may not be obvious why $\mathcal{E}_{<\ell}$ should represent energy at scales smaller than ℓ. Vreman et al. (1994) showed that $\mathcal{E}_{<\ell} \geq 0$ if $G_\ell \geq 0$, whereas $\mathcal{E}_{<\ell}$ can be negative if the coarse-graining kernel G_ℓ is not positive semi-definite. A proof using convexity of the $(\dots)^2$ operation illustrates why the first term $\overline{|\mathbf{u}(\mathbf{x},t)|^2}_\ell$ in eq. (10) has an overbar rather than defining fine KE as $(|\mathbf{u}(\mathbf{x},t)|^2 - |\overline{\mathbf{u}}_\ell(\mathbf{x},t)|^2)/2$. The proof from Sadek and Aluie (2018) is as follows. When using $G_\ell \geq 0$, coarse-graining $\overline{(\dots)}_\ell$ is a local averaging operation. From Jensen's inequality (Lieb & Loss, 2001), we know that $\overline{[\mathcal{F}(\mathbf{u})]}_\ell \geq \mathcal{F}(\overline{\mathbf{u}}_\ell)$ for any convex operation, $\mathcal{F}$. Since $\mathcal{F}(\mathbf{u}) = |\mathbf{u}|^2$ is convex, we are

guaranteed that $\overline{|\mathbf{u}(\mathbf{x},t)|^2_\ell} \geq |\overline{\mathbf{u}}_\ell(\mathbf{x},t)|^2$ and, therefore, $\mathcal{E}_{<\ell} \geq 0$ if the kernel $G_\ell(r) \geq 0$, which is the case for our study (see equation (6)).

Regarding condition (ii) on the sum of energy partitions, Aluie (2019) proved that (for a normalized G_ℓ) the coarse-graining operation on the sphere in equation (1) preserves the spatial average of any field, $\{\overline{F}_\ell(\mathbf{x})\} = \{F(\mathbf{x})\}$, where $\{\dots\} = (Area)^{-1}\int \mathrm{d}\mathcal{S}(\dots)$. Therefore, we have $\left\{\overline{|\mathbf{u}|^2_\ell}\right\} = \left\{|\mathbf{u}|^2\right\}$. This property guarantees that the sum of coarse KE and fine KE yields the total kinetic energy after integrating in space and in the absence of land,

$$\{\mathcal{E}\} = \{\mathcal{E}_\ell\} + \{\mathcal{E}_{<\ell}\}\,. \tag{11}$$

Eq. (11) justifies our interpretation of $\mathcal{E}_{<\ell}$ as energy at scales smaller than ℓ, since it is the difference between bare and coarse kinetic energy, on average, while also being positive locally.

2.3 Treatment of land-sea boundaries

In the above decomposition of energy, a choice has to be made in the presence of land. We here discuss three possibilities along with their pros and cons.

Deformed kernel

The "deformed kernel" approach is realized by coarse-graining ocean points near land with a kernel that is deformed or masked to avoid overlapping with land points. Such a deformed kernel must be renormalized to yield an average over just ocean points rather than the whole sphere. The main advantage of this approach is that it treats land as a well-defined boundary that is separate from the ocean regardless of the coarse-graining length-scale. It is also familiar to ocean modelers who routinely mask values over land and do not include such masked values when performing area averages.

However, the deformed kernel has disadvantages that motivate against its use for coarse-graining ocean flows. First, a kernel that is inhomogeneous (*i.e.* changes shape depending on geographic location) does not conserve domain averages, including the kinetic energy of the flow. The reason for this failed conservation is detailed in Appendix A and demonstrated in Figure 2 (blue plot). This figure shows how a kernel that is deformed (via masking) to exclude land does not yield 100% of the total energy, *i.e.,* it does not satisfy equation (11). As a result, it can yield total energy that is either less than 100% (e.g., over scales larger than 500 km in Figure 2) or *greater* than 100% (e.g., between 100 km and 400 km in Figure 2).

For some purposes, the total energy values in Figure 2 are fairly close to 100% (deviations less than 1%) so one might argue that the deformed kernel is suitable in practice. Nonetheless, a more basic reason to avoid deformed kernels is that such inhomogeneous kernels (which also include averaging values at adjacent grid-cells or block-averaging on the sphere) do not commute with spatial derivatives. Consequently, the coarse-grained field resulting from a deformed kernel is not guaranteed to satisfy fundamental flow properties exhibited by the unaveraged flow, such as incompressibility, geostrophy, and the vorticity present at various scales. These considerations are further detailed in Aluie et al. (2018) and Aluie (2019).

Fixed kernel

The "fixed kernel", also shown in Figure 2, is homogeneous so that it preserves its shape at all locations. When coarse-graining ocean points near land such that the kernel overlaps land points, we treat land points in a manner consistent with the boundary conditions between land and ocean. For example, if we are coarse-graining the velocity, we treat land as water with zero velocity, which is consistent with the formula-

tion of OGCMs where land is often treated as a region of zero velocity. Furthermore, we include these zero land values as part of the coarse-graining operation.

This choice may seem unnatural since we are including unphysical values within the coarse-graining operation. However, it is helpful to think of coarse-graining as an operation analogous to removing one's eyeglasses, rendering an image fuzzy and boundaries less well-defined. When coarse-graining at a scale ℓ, the precise boundary between land and ocean becomes blurred at that scale and its precise location becomes less certain. The coarse-grained velocity, $\overline{\mathbf{u}}_\ell$, can be nonzero within a distance $\ell/2$ beyond the continental boundary over land. Forfeiting exact spatial localization in order to gain scale information is theoretically inevitable due to the uncertainty principle, which prevents the simultaneous localization of data in physical-space and in scale-space (Stein & Weiss, 1971; Sogge, 2008). The main advantage of the "Fixed Kernel" choice is ensuring that coarse-graining and spatial derivatives commute so that it preserves the fundamental physical properties of the flow. Further discussion of these issues can be found in Aluie et al. (2018) and Aluie (2019).

Fixed kernel with or without land

After coarse-graining the velocity field with a fixed kernel, we show in Figure 2 the level of energy conservation if we include or exclude land points from the final tally of kinetic energy. We call these, respectively, the "fixed kernel w/ land" and "fixed kernel w/o land". The latter (orange plot) highlights how coarse-graining smears energy onto land (within $\ell/2$ distance inland) such that if we exclude land from the final tally, we find some leakage of energy onto land, which increases as the coarse-graining scale ℓ increases. We find energy leakage of the order of 1% at coarse-graining scales < 100 km, $\approx 4\%$ for scales $\lesssim 500$ km, and up to 12% at scales of order 2000 km. However, if we choose to include land in our final tally, we are guaranteed to conserve 100% of the energy by satisfying equation (11), thus ensuring that the energy budget is fully closed. After all, in an ocean model on a discrete grid, the land boundary is only expected to be accurate within a Δx distance from any estimate of the truth, where Δx is analogous to our coarse-graining scale ℓ.

What we use here

While we have implemented all three approaches to coarse-graining (see Figure A1 in Appendix A), unless otherwise stated in this work, we choose the fixed kernel w/ land by including land regions that have non-zero velocity (again, as realized through leakage from nearby ocean values). We have checked that our results in all figures shown are almost indistinguishable from choosing fixed kernel w/o land due to the relatively small percentage of energy leakage involved in Figure 2. We avoid coarse-graining with a deformed kernel to remain consistent with previous work Aluie et al. (2018) and with forthcoming studies where we apply coarse-graining to the dynamical equations where commuting with spatial derivatives is essential.

2.4 The filtering spectrum

Sadek and Aluie (2018) showed how coarse-graining can be used to extract the energy content at different length scales. They do so by partitioning the velocity into discrete length scale bands rather than the two sets (coarse KE and fine KE) in equations (9) and (10). The resulting quantity is called the *filtering spectrum*. The filtering spectrum is distinct from the traditional Fourier spectrum, with coarse-graining offering a way to measure energy distributions without relying on a Fourier transform, thus avoiding the limitations noted in Section 1.1.

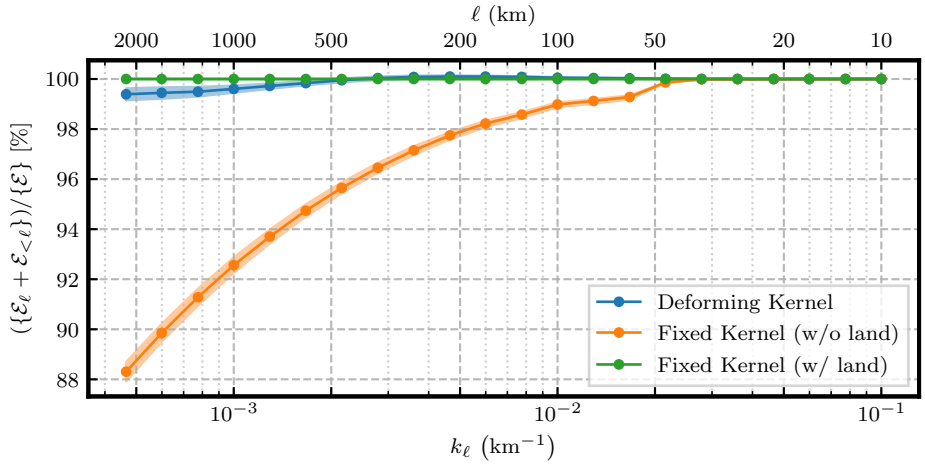

Figure 2. Percentage of total energy recovered by summing the fine and coarse KE terms in equation (11) obtained by coarse-graining over the full ocean surface as a function of the filter scale, $k_\ell = 1/\ell$. The three lines correspond to the three approaches described in section 2.3, namely, filtering with a fixed kernel shape and excluding/including land (orange/green lines) when tallying the total energy. We also coarse-grain with a deformable filter kernel to exclude the filter overlapping land regions (blue line).

The filtering spectrum is obtained by differentiating in scale the coarse KE

$$\overline{E}(k_\ell) = \frac{d}{dk_\ell}\{\mathcal{E}_\ell\} = -\ell^2 \frac{d}{d\ell}\{\mathcal{E}_\ell\}\,, \tag{12}$$

where $k_\ell = 1/\ell$ is the 'filtering wavenumber.' Sadek and Aluie (2018) showed that $\overline{E}(k_\ell, t) \geq 0$ when using certain types of kernels (e.g., concave) of which the top-hat kernel is an example. Moreover, Sadek and Aluie (2018) identified the conditions on G_ℓ for $\overline{E}(k_\ell, t)$ to be meaningful in the sense that its scaling agrees with that of the traditional Fourier spectrum (when a Fourier analysis is possible, such as in periodic domains). Below, we shall sometimes refer to $\mathcal{E}_\ell$ as the "cumulative spectrum" following Sadek and Aluie (2018) since it accounts for all energy at scales larger than ℓ. In contrast, $\overline{E}(k_\ell, t)$, is the spectral energy *density* at a specific scale ℓ.

2.5 Reynolds averaging

We close this section by reviewing basic properties of Reynolds averaging (RA) as realized by time averages.

Basics of Reynolds averaging

Time averaging separates the flow into a time-average/'mean' and a fluctuating/'eddy' as given by (Pope, 2001)

$$\langle \mathbf{u} \rangle(\mathbf{x}) = \frac{1}{T}\int_{t_0}^{t_0+T} \mathbf{u}(\mathbf{x}, t)\mathrm{d}t, \tag{13}$$

$$\mathbf{u}'(\mathbf{x}, t) = \mathbf{u}(\mathbf{x}, t) - \langle \mathbf{u} \rangle(\mathbf{x}), \tag{14}$$

where $\langle \mathbf{u} \rangle$ is the mean component, $\mathbf{u}'$ the eddy component, and T represents the entire time record and not just a time window. Two key properties of the Reynold's decomposition are

$$\langle \langle \mathbf{u} \rangle \rangle = \langle \mathbf{u} \rangle \quad \text{and} \quad \langle \mathbf{u}' \rangle = 0, \tag{15}$$

so that the mean of a mean returns the mean (idempotence property) while the mean of the eddy is zero. The resulting mean and eddy kinetic energy components are respectively given by

$$MKE(\mathbf{x}) = \frac{1}{2}|\langle \mathbf{u} \rangle|^2(\mathbf{x}), \tag{16}$$

$$EKE(\mathbf{x}, t) = \frac{1}{2}|\mathbf{u}'|^2(\mathbf{x}, t). \tag{17}$$

Notice that the sum of mean and eddy kinetic energy is not equal to the total kinetic energy. Rather, there is an extra cross term, $\mathbf{u}' \cdot \langle \mathbf{u} \rangle$, needed to close the budget. However, the cross term is not positive definite and it has a zero time average, $\langle \mathbf{u}' \cdot \mathbf{u} \rangle = 0$. Following a RA decomposition, the total energy can be written as

$$\mathcal{E}(\mathbf{x}, t) = EKE(\mathbf{x}, t) + MKE(\mathbf{x}) + \frac{1}{2}\left(\mathbf{u}' \cdot \langle \mathbf{u} \rangle\right)(\mathbf{x}, t). \tag{18}$$

Key differences between Reynolds averaging and coarse-graining

A key difference between coarse-graining and Reynolds-averaging is that within RA, applying the averaging operation twice on any field yields the same result whereas that property does not hold for coarse-graining with non-projector kernels (Buzzicotti et al., 2018)

$$\langle \langle F \rangle \rangle = \langle F \rangle \quad \text{whereas} \quad \overline{\overline{F}} \neq \overline{F}. \tag{19}$$

Another important difference is that a Reynolds average does not provide a control to adjust the partition between the "mean" and "eddy" components. That is, a Reynolds decomposition is not a length-scale decomposition and this point is illustrated in section 4.5 (see Figure 11). Consequently, the time-mean flow is not synonymous with large-scale flow, nor does a Reynolds eddy fluctuation directly correspond to a characteristic fine-scale.

To help understand the above points, we emphasize the distinction between time-scale and decorrelation-time for a particular flow feature. While it is generally true that larger (smaller) scales have slower (faster) time-scale dynamics, it is not always true that their decorrelation-time follows this relation. As an example, consider stationary eddies, such as the Mann eddy in the North Atlantic. Such eddies have a small spatial-scale (relative to the gyre or basin) but are persistent in time. As a result, even if the timescale ($\sim \ell/u$) for a structure is small when it is associated with the relatively fast dynamics of eddying flows, it can be highly correlated (or even stationary) in time, so that its contribution to the MKE is not completely removed by a time-average. We show this behavior in sections 4.5 and 4.6.

3 Satellite and numerical model data

We examine the horizontal geostrophic velocity of surface ocean currents from a global numerical model simulation and from an analysis of satellite sea surface altimetry, focusing on regions to the north and south of the tropics, [15°N−90°N] and [15°S−90°S], as depicted in Figure 3. We avoid the tropics since our interest is with the geostrophic flows in the higher latitudes, and only the surface geostrophic current is available from satellite altimetry. Details of the two products are given in the following subsections, and both were publicly accessed through the Copernicus Marine Environment Monitoring Service (CMEMS) webpage.

3.1 AVISO analysis of satellite altimetry

Geostrophic currents are obtained from the AVISO+ analysis of multi-mission satellite altimetry measurements for sea surface height (SSH) (Pujol et al., 2016). We used the Level 4 (L4) post-processed dataset of daily-averaged geostrophic velocity, gridded

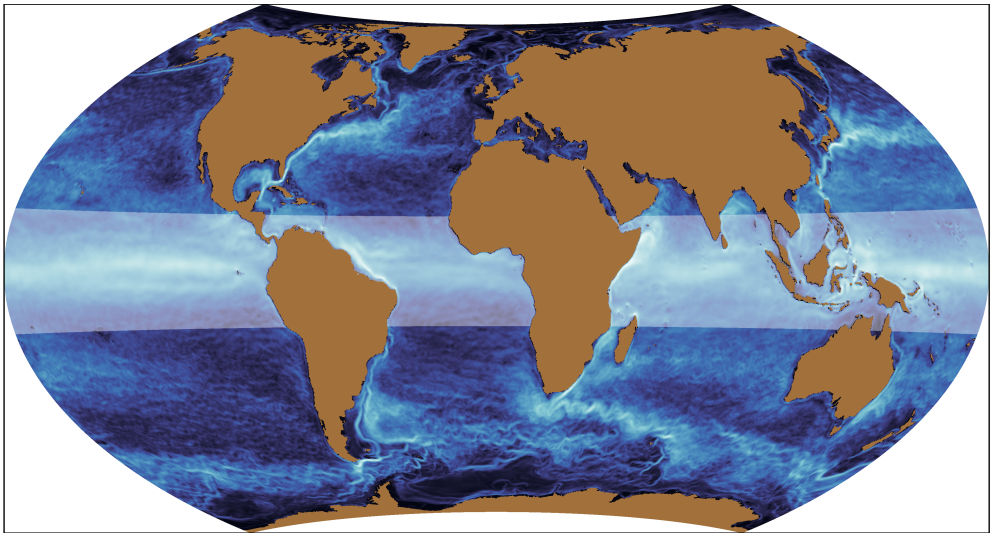

Figure 3. Geographic regions considered in this analysis. The shaded area between $[15°\text{S} - 15°\text{N}]$ is the tropical band that is neglected in this work. We instead consider the geostrophic flow in the higher latitudes. Visualization shows a one-year time average of the full kinetic energy from NEMO for illustration.

at a resolution of $0.25° \times 0.25°$ and spanning from January 2010 to October 2018. Post processing was performed by the Sea Level Thematic Center (SL TAC) data processing system, which processes data from eleven altimeter missions.

The product identifier of the AVISO dataset used in this work is "SEALEVEL_GLO_PHY_L4_REP_OBSERVATIONS_008_047", and can be downloaded at `https://marine.copernicus.eu/services-portfolio/access-to-products/`.

3.2 Numerical simulation

We analyze 1-day averaged surface geostrophic currents from the NEMO numerical modeling framework, which is coupled to the Met Office Unified Model atmosphere component, and the Los Alamos sea ice model (CICE). The NEMO dataset consists of weakly coupled ocean-atmosphere data assimilation and forecast system, which is used to provide 10 days of 3D global ocean forecasts on the same grid of 0.25 degree spacing. We use daily-averaged data that spans three years, from 2016 to 2019. More details about the coupled data assimilation system used for the production of the NEMO dataset can be found in (Hewitt et al., 2011; Lea et al., 2015). The specific product identifier of the NEMO dataset used in this work is "GLOBAL_ANALYSISFORECAST_PHY_CPL_001_015", and it can be downloaded from CMEMS at `https://marine.copernicus.eu/services-portfolio/access-to-products/`.

4 Analysis results

In this section we present results of the coarse-graining analysis along with a comparison with Reynolds averaging based on time averages. In the second part of this section we present results from coarse-graining in both space and in time as a means to characterize the time-scales associated with different length-scales.

4.1 Coarse-graining the surface geostrophic flow from AVISO

We split the geostrophic kinetic energy from AVISO into its fine and coarse-grained components following equations (9) and (10). For a qualitative appreciation of this decomposition, Figure 4 displays maps of the kinetic energy just over the Atlantic using two different filter scales, $\ell = 100$ km in the top row and $\ell = 400$ km in the bottom row. From left to right, panels in Figure 4 show the total kinetic energy, $\mathcal{E}$, the coarse energy, $\mathcal{E}_\ell$, and the fine energy, $\mathcal{E}_{<\ell}$. The fine scale kinetic energy, $\mathcal{E}_{<\ell}$, represents kinetic energy at scales less than ℓ, as represented (or projected) on a grid of resolution $\Delta x \sim \ell$. Notably, as seen in Figure 4, $\mathcal{E}_{<\ell}$ does not have small scale features, which results since there is a filter applied to both terms in equation (10) defining $\mathcal{E}_{<\ell}$. This definition ensures that $\mathcal{E}_{<\ell}$ is positive semi-definite at each point in space and time.

Visualization of fine kinetic energy, $\mathcal{E}_{<\ell}$, is still useful to identify the regions where it is dominant in the ocean. Even so, one may wish to view the alternative quantity

$$\mathcal{E} - \mathcal{E}_\ell = \frac{1}{2}\left(|\mathbf{u}(\mathbf{x},t)|^2 - |\overline{\mathbf{u}}_\ell(\mathbf{x},t)|^2\right), \tag{20}$$

which is shown in the right-most column of Figure 4. This quantity reveals more fine scale features since only the second term on the right hand side is filtered. However, as discussed in Section 2.1, the energy difference, $\mathcal{E} - \mathcal{E}_\ell$, can be negative locally in space, and so it does not serve our purposes for decomposing the energy into non-negative terms.

4.2 Seasonality of the fine scale geostrophic kinetic energy

In Figure 5, we present the seasonality of the fine scale geostrophic kinetic energy in the North (solid lines) and South (dashed lines). We show results just from AVISO, though note that similar results hold for the NEMO output. Figure 5 shows the calculation of fine scale kinetic energy with four different filter scales, $\ell = 77$ km, 129 km, 215 km, and 464 km. We choose these length-scales due to their equal spacing on a logarithmic scale.

The fine scale geostrophic kinetic energy in Figure 5 reveals a clear seasonality across all length scales, generally peaking in the spring and attaining a minimum in the autumn of both hemispheres. The study of Qiu et al. (2014) and Steinberg et al. (2021) arrive at a similar conclusion about seasonality using different methods. The cause for such seasonality is an ongoing topic of research, requiring the analysis of various mesoscale sources and sinks. Rai et al. (2021) recently showed that eddy-killing is a significant global mesoscale sink with a seasonal cycle that peaks in winter, thereby offering a potential explanation for mesoscale seasonality. Another possible explanation was put forth by Qiu et al. (2014), who showed evidence for seasonality in the upscale energy cascade in the North Pacific. While it is beyond the scope of this paper, it is worth noting that, in addition to highlighting seasonal variations, the bottom panel of Figure 5 reveals a general increase in mesoscale energy over the plotted timeframe. This long-term increase is present in both the North of Tropics and South of Tropics regions and is consistent with recent analysis by Martínez-Moreno et al. (2021).

In the middle panel in Figure 5 we show the fine scale kinetic energy normalized as a percentage of the total energy, $\{\mathcal{E}_{<\ell}\} / \{\mathcal{E}\}\,(t)$. From this plot we can see that along the full time series, more than 90% of the total geostrophic kinetic energy resides at scales $\lesssim 500$ km and a large percentage ($\approx 60\%$) is contained between ≈ 100 and ≈ 500 km, which can be identified as the bulk of the geostrophic flow.

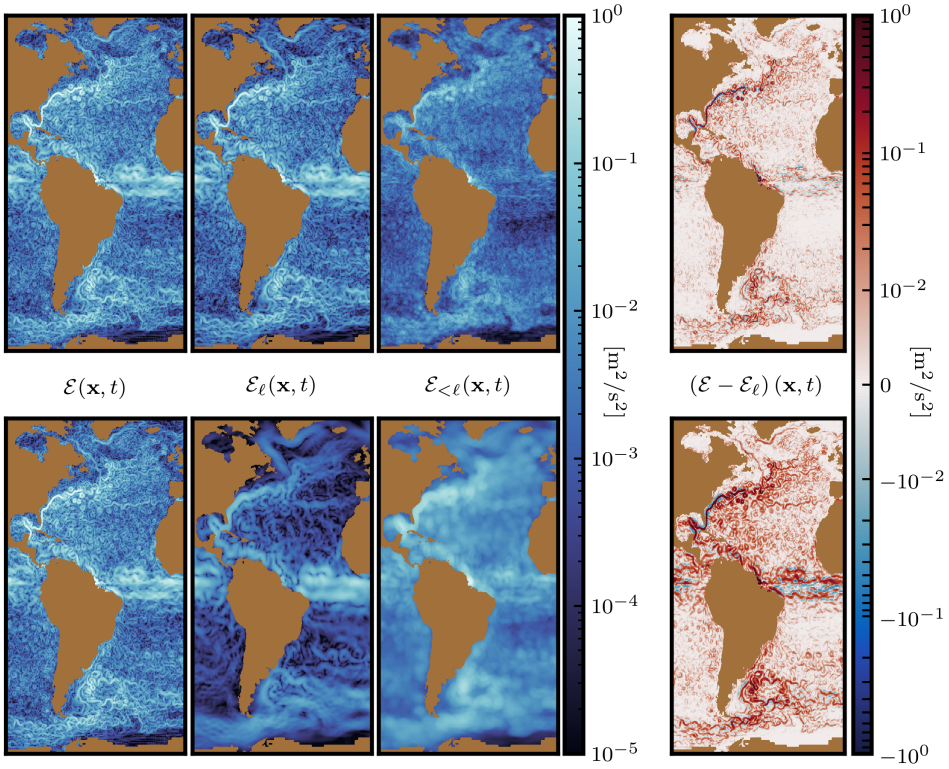

Figure 4. Maps of the coarse-grained decomposition of kinetic energy performed on a single-day from the AVISO analysis at two different filter scales, $\ell = 100$ km (top row) and $\ell = 400$ km (bottom row). Here the bare KE, $\mathcal{E}(\mathbf{x},t)$, is compared with coarse KE, $\mathcal{E}_\ell(\mathbf{x},t)$, and fine KE, $\mathcal{E}_{<\ell}(\mathbf{x},t)$. The right-most column shows the resulting fine scale term defined by equation (20), which can yield values that are negative.

4.3 The filtering spectrum

In Figure 6 we show the filtering spectrum for the global ocean surface geostrophic kinetic energy as obtained from equation (12) for both AVISO and NEMO. In the left panel we show the cumulative energy spectra, $\mathcal{E}_\ell$, as a function of coarse-graining scale, ℓ. These results highlight those from Figure 5, revealing that the overwhelming contribution to geostrophic kinetic resides at length-scales $\ell < 500$ km. Based on prior characterization of ocean energetics (Ferrari & Wunsch, 2009), we assume that this length scale is dominated by mesoscale features such as geostrophic turbulence, boundary currents, and fronts. Hence, our analysis provides further compelling evidence for dominance of the ocean surface kinetic energy by mesoscale flows.

In the right panel of Figure 6, we show the actual filtering spectrum, which is the derivative (in scale) of the corresponding plot in the left panel. We can see a peak centered at $\ell \approx 300$ km, with the bulk of the geostrophic kinetic energy residing between scales 100 km and 500 km. From the analysis shown in Figure 6, we find that $60 \pm 0.4\%$ of the kinetic energy in the extra-tropics from the AVISO and NEMO products lies within the 100 km to 500 km scale-band. Again, Figure 6 provides compelling evidence that the mesoscales in the extra-tropical latitudes constitute the most energetic component of the oceanic circulation.

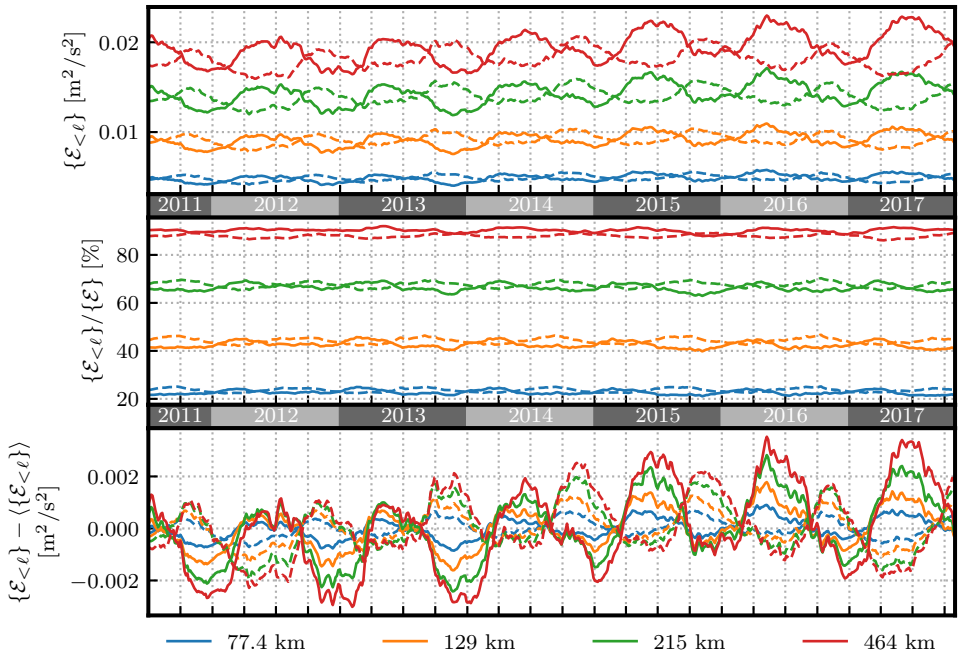

Figure 5. Top panel: Time-series of fine scale geostrophic kinetic energy, $\mathcal{E}_{<\ell}$, representing energy at scales smaller than ℓ, in the North (solid lines) and South (dashed lines) obtained from the AVISO analysis. Different colors indicate different scales ℓ. Middle panel: The same time-series, but now normalized by the original kinetic energy, $\mathcal{E}$, to show the % of kinetic energy residing at scales $< \ell$. Bottom panel: deviation of $\mathcal{E}_{<\ell}$ from the time-mean value to emphasize seasonal variability. Vertical grid lines indicate the start of each quarter-year (01Jan, 01Apr, 01Jul, 01Oct). We see that the mesoscales exhibit a seasonal oscillation that generally peaks in the spring, and that they account for a dominant fraction of the total geostrophic kinetic energy. Here, we show only 6.5 years of the 9-year record analyzed with a 4-day sampling, but averages are based on a 1-day sampling.

If we focus on each hemisphere separately, we find that the 100 km to 500 km scale-band comprises $62 \pm 1\%$ of the North's kinetic energy and $58 \pm 1\%$ of the South's kinetic energy. Indeed, one can notice slight differences between the North's and South's spectra in Figure 6 (right panel), where the South has relatively more energy at scales larger than 1000 km. This bias can be attributed to the large-scale contribution from the Antarctic Circumpolar Current. On the other hand, the North has slightly more kinetic at scales within the 100 km to 1000 km range, which can be attributed to boundary currents (Kuroshio and Gulf Stream). In support of our assertion, consider Fig. 7, which shows the zonally-averaged kinetic energy for selected length-scale bands. Scales larger than 1000km (blue plot in Fig. 7) have a dominant contribution from latitudes [60°S, 40°S], which roughly corresponds with the Antarctic Circumpolar Current. However, these latitudes are no longer dominant when considering the band of smaller scales: 215 km $< \ell <$ 1000 km. These scales (orange plot in Fig. 7) show a distinct signal at latitudes [30°N, 40°N], which roughly aligns with the Gulf Stream and Kuroshio. There is also a weaker signal at latitudes [40°S, 35°S], with roughly aligns with the Agulhas and the Brazil-Malvinas currents.

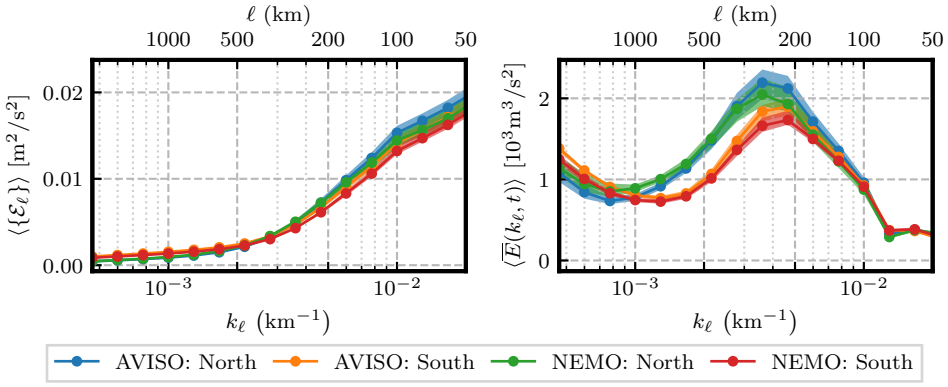

Figure 6. Left panel: Cumulative surface geostrophic kinetic energy spectra, $\mathcal{E}_\ell$, as a function of scale ℓ, obtained from both the AVISO and NEMO products in the North and South. Right panel: Filtering spectra obtained as a derivative with respect to $k_\ell = 1/\ell$ of the corresponding cumulative energy spectra showed in the left panel (see equation (12)). Envelopes show inter-quartile range (25th to 75th percentiles) of temporal variation. Note that the bulk of surface geostrophic kinetic energy resides at scales within the 100 km to 500 km range.

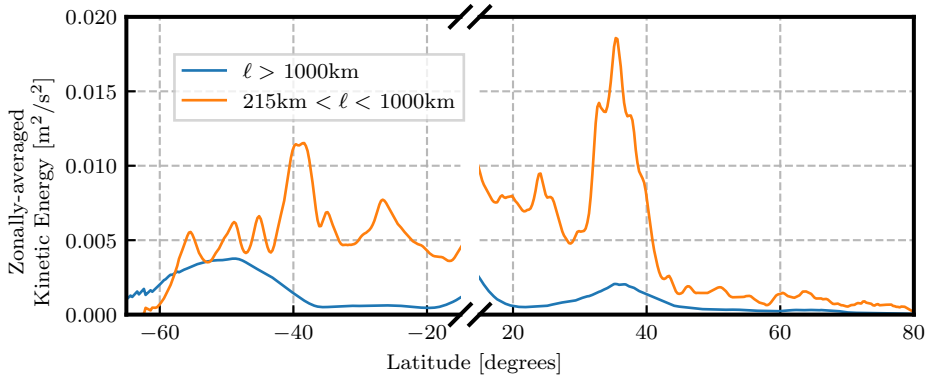

Figure 7. Time- and zonally-averaged kinetic energy computed from AVISO within selected length-scale bands (see in-set legend) as a function of latitude. We can see that the Antarctic Circumpolar Current has significant energy at scales > 1000 km, while the North has significant energy within $\approx 30°$N-40°N where the Western Boundary Currents are located. Note that the latitude axis is broken to exclude the band [15°S, 15°N].

4.4 Reynolds averaging decomposition

In this subsection and the next, we show that the time-mean flow consists of an entire range of length scales with substantial contributions from the mesoscale. Figure 8 shows the mean-fluctuation decomposition following the Reynolds averaging approach. The maps are focused on the Atlantic region to help reveal details and we show just those obtained from AVISO. The time mean is obtained by averaging the velocity over the whole time series available, spanning nine years. From left to right we show the total energy at a single day, the time mean energy, $MKE(\mathbf{x})$, the fluctuating eddy term, $EKE(\mathbf{x}, t)$, and the cross term, $1/2(\mathbf{u}' \cdot \langle\mathbf{u}\rangle)$.

Having used a relatively long time series for averaging, the mean energy in Figure 8 is rather depleted away from major current systems, so that the Gulf Stream

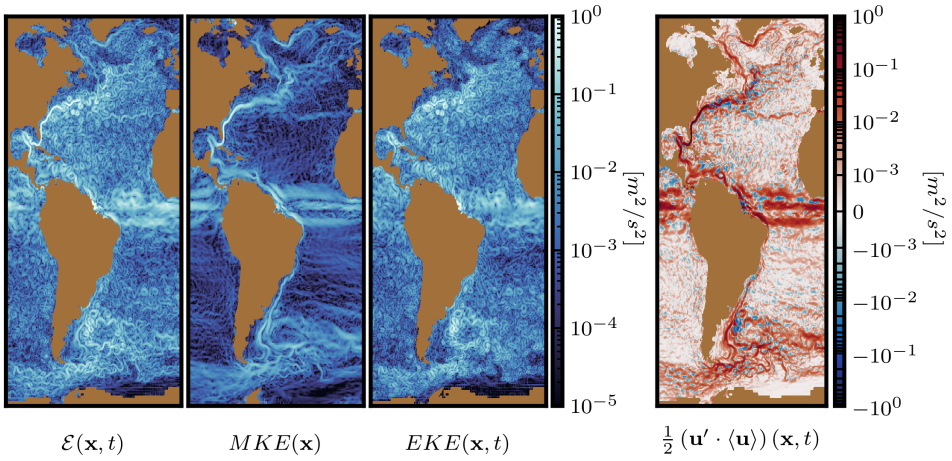

Figure 8. Decomposition of geostrophic kinetic energy from AVISO for the Atlantic basin from a time averaging (Reynolds) decomposition. Left panel: total energy, $\mathcal{E}(\mathbf{x},t)$ at a single day. Left middle panel: 9-year time mean, $MKE(\mathbf{x})$. Right middle panel: fluctuating eddy term, $EKE(\mathbf{x},t)$. Right panel: the cross term required to recover the total geostrophic energy as defined in equation (18). Note that $MKE(\mathbf{x})$ contains small length-scales and EKE contains a large-scale component of the flow.

and the Antarctic Circumpolar Current are quite pronounced relative to the gyre interiors. We appreciate from this figure that the mean flow retains a substantial contribution from structures with a variety of sizes. In the same way, the 'eddy' (or temporally fluctuating) flow in Figure 8 contains most of the small scale fluctuations but also a substantial contribution from large-scale structures. The cross term shown on the right panel of Figure 8 has strong fluctuations around zero, which make its contribution almost (but not exactly) zero after a spatial-average. The blending of length scales revealed by these figures reflects the inability of time averaging to decompose the kinetic energy according to length-scales.

To further investigate the role of the three Reynolds average energy terms, Figure 9 shows their temporal variability in both hemispheres. In the first row, we see that EKE constitutes a substantial portion of the total energy $\mathcal{E}$ (80%) and their temporal evolution is almost indistinguishable. Both EKE and $\mathcal{E}$ tend to peak during the spring-summer. The bottom row of Figure 9 shows MKE, which is independent of time, and the cross term, which has a zero average. These two quantities are much less energetic, with the mean term $\approx 20\%$ of the total and the cross term fluctuates about its zero average without a clear seasonal signal.

4.5 Spatio-temporal decomposition

In this section we present results from coarse-graining in both space and time to reveal the time-scales of various length-scales, including length-scales present in the 9-year temporal mean. Our analysis demonstrates a new way for comparing data from satellite analysis (AVISO) and numerical models (NEMO).

The approach consists of measuring the filtering spectrum of a temporally-smoothed version of the original velocity field. The latter is obtained from a running

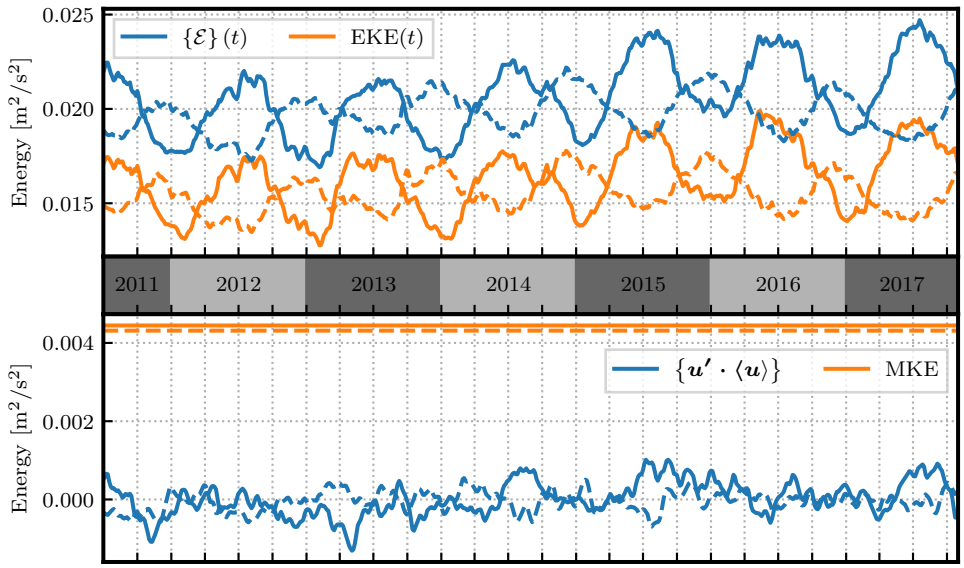

Figure 9. Top panel: Time-series of total geostrophic kinetic energy, $\{\mathcal{E}(t)\}$ (blue), and the fluctuating component, $\{EKE(t)\}$ (orange), in the North (solid line) and South (dashed line) from the AVISO analysis. Vertical grid lines indicate the start of each quarter-year (01Jan, 01Apr, 01Jul, 01Oct). Bottom panel: Time-series of the cross term (blue) and kinetic energy of the 9-year mean, $\{MKE(\mathbf{x})\}$ (orange), in the North (solid line) and South (dashed line). EKE constitutes a substantial portion of the total energy and with an almost indistinguishable temporal variation. Here, we show only 6.5 years of the full 9-year record. Plots shown use a 4-day sampling frequency, but averages are based on a 1-day sampling of the 9-year record.

window time-average,

$$\langle \mathbf{u} \rangle_\tau(\mathbf{x}, t) = \frac{1}{\tau} \int_{t-\tau/2}^{t+\tau/2} \mathbf{u}(\mathbf{x}, t')\, \mathrm{d}t', \tag{21}$$

with τ the size of the time window. Note that a running window time-average in equation (21) is similar to spatial coarse-graining (equation (1)) since

$$\langle \langle F \rangle_\tau \rangle_\tau \neq \langle F \rangle_\tau, \tag{22}$$

so that it does not satisfy the Reynolds averaging idempotent property, $\langle \langle F \rangle \rangle = \langle F \rangle$.

Combining equation (12) with equation (21) allows us to measure the filtered energy spectrum of the time smoothed field

$$\overline{E}(k_\ell, \tau) = \langle \frac{d}{dk_\ell} \{ \frac{1}{2} |\langle \overline{\mathbf{u}}_\ell \rangle_\tau|^2 \} \rangle = \langle \frac{d}{dk_\ell} \{ \mathcal{E}_{\ell,\tau} \} \rangle, \tag{23}$$

where we introduced

$$\mathcal{E}_{\ell,\tau}(\mathbf{x}, t) = \frac{1}{2} |\langle \overline{\mathbf{u}}_\ell \rangle_\tau|^2, \tag{24}$$

which is the cumulative spectrum of the temporally-smoothed field. As indicated, $\mathcal{E}_{\ell,\tau}(\mathbf{x}, t)$ is a function of both the size of the time-window, τ, and the inverse coarse-graining scale, $k_\ell = \ell^{-1}$.

We show the time-smoothed energy map, $\mathcal{E}_{\ell=0,\tau}$, in Figure 10 from AVISO. Here, the two columns compare results from the North and the South regions, while different rows compare results with different time windows, τ. From these maps we

can see that increasing τ from one day to 1093 days reduces the energy down to $\approx 21\%$ ($\approx 25\%$) of the original total energy in the North (South). Hence, averaging over three years brings the energy down to values comparable to those over the full nine years obtained in the previous section by the Reynolds averaging decomposition, where we found that MKE accounts for $\approx 20\%$ of the total energy in the extra-tropics. This result indicates that temporal averaging converges quickly for the geostropphic kinetic energy, and using longer time records does not significantly alter the partitioning between the temporal mean and fluctuating components of the surface geostrophic ocean flow.

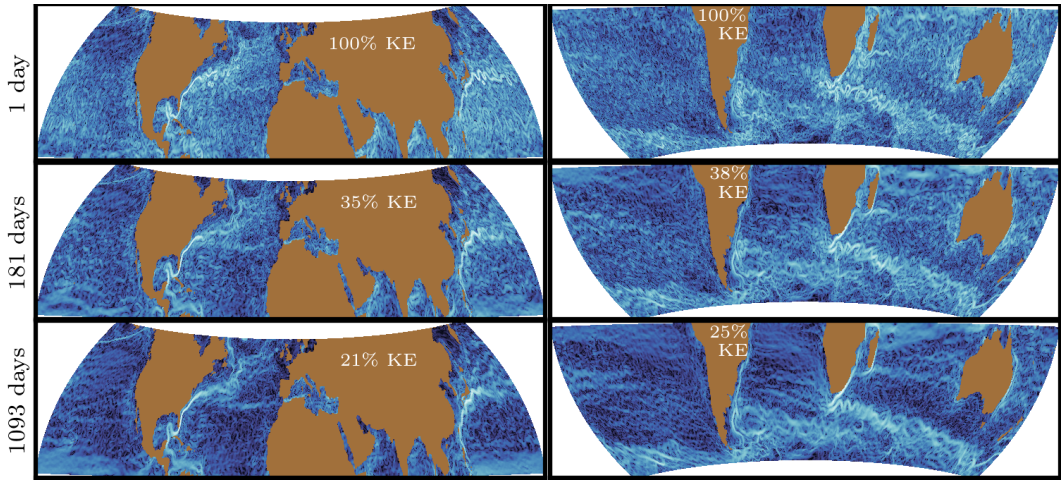

Figure 10. The surface geostrophic kinetic energy from the temporally coarse-grained flow, $\mathcal{E}_{\ell=0,\tau}$, in the North (left column) and South (right column) from AVISO. The top row shows the original 1-day averaged flow. The middle and bottom rows show the kinetic energy from the flow when averaged with a ≈ 6 months time window and a ≈ 3 years time window, respectively, with the kinetic energy decreasing with an increasing time window. Each panel indicates the % of kinetic energy remaining relative to the 1-day top row.

In Figure 11 we show the filtering spectra of the temporally-smoothed flow, $\overline{E}(k_\ell, \tau)$. The top panel shows the filtering spectra $\overline{E}(k_\ell, \tau)$ as a function of k_ℓ for various values of τ. Bottom panel shows the same quantities, but normalized by $\overline{E}(k_\ell, \tau = 0)$, which is the spectrum of the flow without temporal coarse-graining. From this analysis, we find that the main effect of the temporal coarse-graining is to make the energy peak around $\ell \approx 300$ km less pronounced, with the consequence of having a spectral energy distribution that is more evenly distributed across length-scales than in the original flow. Indeed, we can see from Figure 11 (bottom panel) that time averaging removes energy at all scales. As we increase the time window τ, $\overline{E}(k_\ell, \tau)$ at scales $\lesssim 300$ km appears to mostly shift downward in equal proportion. This behavior is counter to the notion that smaller scales decorrelate faster in time and are removed more efficiently with time-averaging.

From Figure 11, we see that as the time window $\tau \to \infty$, $\overline{E}(k_\ell, \tau)$ converges to the time-mean spectrum (dashed plot in Figure 11), which highlights that the 9-year mean flow consists of an entire continuum of length-scales. The spectrum of the 9-year mean flow shows a reduction of $\approx 20\%$ of the total at the largest scales of > 1000 km (bottom panel in Figure 11). Our analysis of Figure 11 (dashed line), allows us to infer that roughly 60% of the kinetic energy in the 9-year time-mean is at

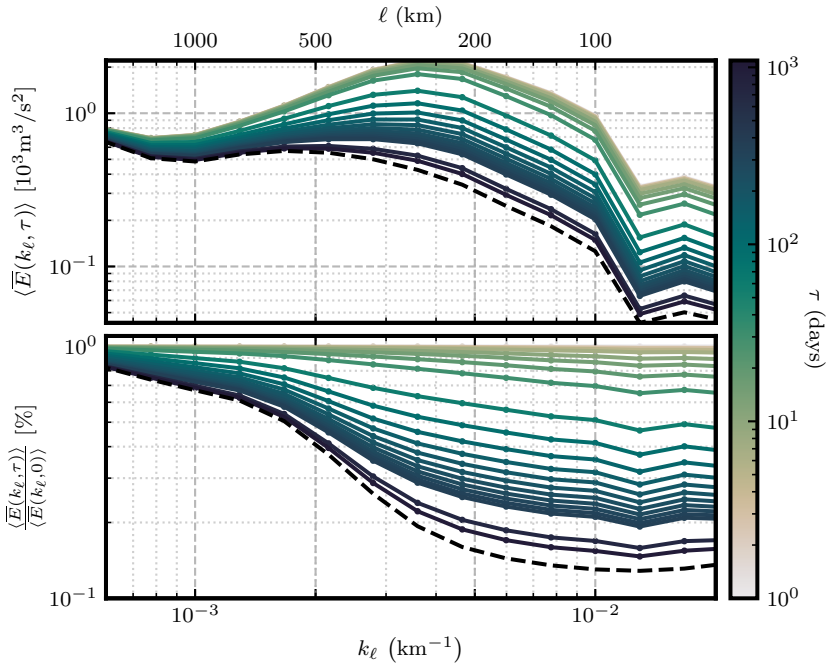

Figure 11. Top panel: Kinetic energy spectra as a function of spatial scale, $k_\ell = 1/\ell$, of the temporally smoothed velocity field, $\overline{E}(k_\ell, \tau)$, in the North from AVISO. Colours indicate the time-window size τ used in the smoothing procedure, ranging from 1 day (pale yellow colour) up to 1000 days (dark green). Bottom panel: The same spectra but now normalized by $\overline{E}(k_\ell, \tau = 0)$, which is the spectrum of the flow without temporal smoothing. In both panels the dashed lines represent the spectra of the mean energy obtained via the Reynolds averaging decomposition, from which we find that 70% of energy in the time-mean flow in the North is at scales < 500 km (55% in the South, not shown).

scales < 500 km outside the $[15°\text{S} - 15°\text{N}]$ band, underscoring the poor association between temporal averaging and length-scales.

4.6 Spatio-temporal comparison of AVISO and NEMO

We now demonstrate a new method to compare data from satellite analysis (AVISO) and numerical models (NEMO) by using a spatio-temporal coarse-graining to identify inconspicuous flow properties or artifacts, and may complement current efforts to disentangle balanced from unbalanced motions in SSH-derived flows. Figure 12 presents space-time 2-D spectra, $-\langle \frac{d}{d\tau}\frac{d}{dk_\ell}\{\mathcal{E}_{\ell,\tau}\}\rangle$, which decomposes the energy as measured from AVISO and NEMO. In the main panel of Figure 12 we show the isolevels of space-time spectra from AVISO (blue lines), superposed onto those from NEMO (red lines). Here, the color intensity is proportional to the energy as indicated by the colorbar in Figure 12. At the side of the main panel we show the one dimensional energy spectra as a function of time, τ, and scale, ℓ. The most striking difference is that AVISO isolines (blue) are concentric circles with a peak at $\tau \approx 20$ days and $\ell \approx 300$ km, while NEMO isolines (red) resemble horseshoes with a peak that encompasses shorter time-scale $\tau \leq 20$ days and a wider range of length-scales. The right panel in Figure 12 plots $-\langle \frac{d}{d\tau}\{\mathcal{E}_{\ell=0,\tau}\}\rangle$, underscoring the difference between AVISO and NEMO spectra, which disagree significantly over time-scales smaller than ≈ 10 days. Note that the top panel in Figure 12, which compares

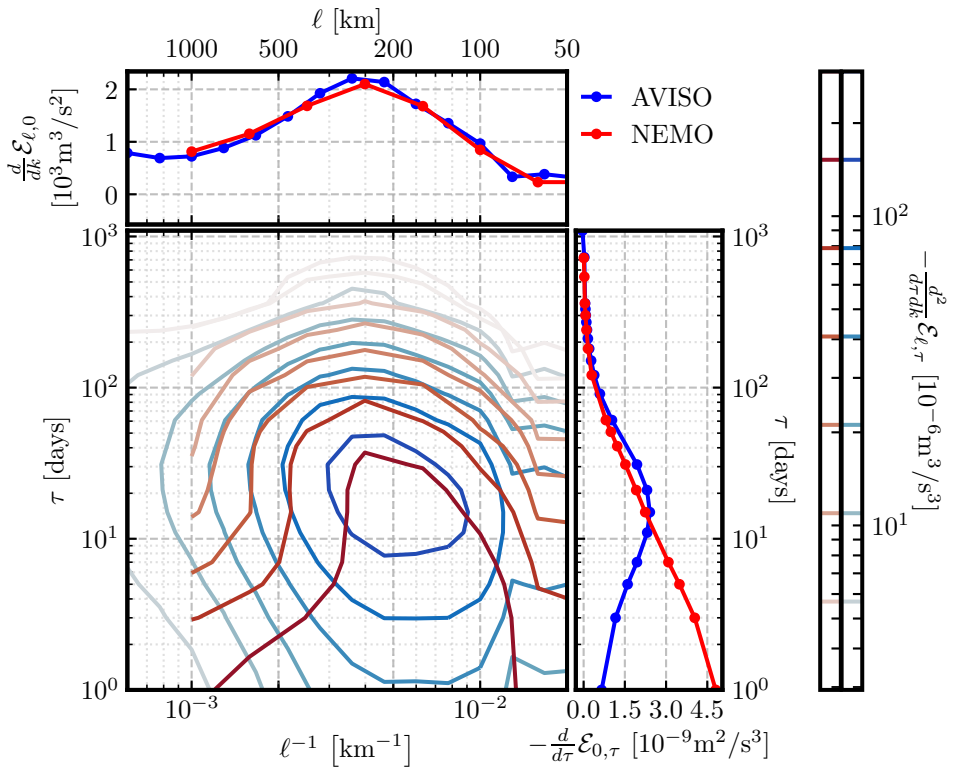

Figure 12. Combined spatio-temporal coarse-graining shows space-time 2D spectra, $-\partial_\tau \partial_{k_\ell} \mathcal{E}_{\ell,\tau}$, (central panel) from AVISO (blue isolines) and NEMO (red isolines). Right (top) panel shows energy spectra as a function of time-scale τ (length-scale $k_\ell = 1/\ell$). Spatio-temporal spectral isolines from AVISO are concentric circles with a peak around $\tau \approx 20$ days and $\ell \approx 300$ km while those from NEMO (red isolines) are horseshoe-like with a peak encompassing smaller time-scales. AVISO mis-represents time-scales $\lesssim 10$ days over all length-scales.

spectra of spatial scales, shows very good agreement and, without a temporal decomposition, it fails to detect the disagreement in time-scales that exist over a wide range of spatial scales, from $\ell \approx 100$ km to 1000 km (main panel in Figure 12).

Remember that for the entire analysis in this paper, we are using 1-day averages of SSH to derive velocity from the NEMO data. While the SSH from AVISO is also available daily, it is effectively averaged over longer periods of time to produce gridded SSH maps from along-track altimeter data. We hypothesize that the difference between isocontours from AVISO and NEMO in Figure 12 comes from the optimal interpolation used to produce the gridded AVISO product (Pujol et al., 2016), which is necessary to construct the global maps from satellite altimeters' along-track data. To support this hypothesis, in Figure 13, we show the spectra as a function of τ measured from AVISO and NEMO. In this plot we have repeated the analysis of the NEMO spectra after passing the data through a 7-day running time-average (green line), which reproduces the time average over the satellite orbits. We can see that the green curve overlaps the AVISO measurement (blue) very closely, supporting our hypothesis. This is similar to what was done in Arbic et al. (2014); Khatri et al. (2018) who were comparing the cascade from AVISO and model data and determined that AVISO's spectral fluxes can be reproduced from model data after filtering the latter in both space and time.

What component of the flow could be yielding the discrepancy between NEMO and AVISO? The most obvious possibility is unbalanced motion present in the 1-day mean SSH fields of NEMO that is absent from AVISO due to the effective weekly averaging required for gridding the satellite measurements. However, unbalanced motion had been believed to be important mostly over length-scales $\lesssim$ 100 km and time-scales $\lesssim$ 2 days (e.g. Richman et al. (2012); Qiu et al. (2018)). If our conjecture is correct, it would imply that unbalanced motion is present at all scales and is significant even at scales between 200 km to 1000 km, requiring averaging over a few days to be removed. Isolating balanced from unbalanced motions (e.g. Bühler et al. (2014)) is an active research topic that is beyond the scope of this work.

Figure 12 shows the importance of performing a combined spatio-temporal decomposition to access all information in the data. Our method is similar to frequency-wavenumber analysis performed within Fourier boxes by several recent studies: Arbic et al. (2014) were interested in mesoscale-driven intrinsic low-frequency variability, while Savage et al. (2017); Qiu et al. (2018); Torres et al. (2018) were primarily motivated by isolating the unbalanced motions from SSH-derived velocities. Our Figure 12 is analogous, for example, to Figure 4 in Arbic et al. (2014) and to Figure 3 in Torres et al. (2018). However, as we mentioned in the introduction, the coarse-graining approach gives us access to the *global* energy budget and, moreover, frees us from the limitations of Fourier boxes and the required tapering and detrending. As such, the approach here complements previous frequency-wavenumber analysis by allowing us to access much larger length-scales.

A common feature between our Figure 12 and those in previous studies is a slight elongation of iso-contours along the diagonal from small to large spatio-temporal scales in the main panel of our Figure 12. Such elongation is most prominent in Figure 3 of Torres et al. (2018), who were probing scales $<$ 100 km and from roughly 3 hours to 40 days. The diagonal elongation of isocontours represents a slight tendency for larger length-scales to have longer time-scales.

However, we emphasize that unlike in Torres et al. (2018), such tendency is only *slight* over the larger scales we analyze here. In fact, an important take-away from Figure 12 is that all length-scales evolve over a wide range of time-scales, consistent with plots in Figure 11. Consider, for example, $\ell \approx 500$ km in the main panel of Figure 12 at different τ values. We see that the (red) isoline is almost vertical over $\tau \approx 5$ days to $\tau \approx 50$ days, indicating that flow at 500 km has an equal contribution from all these time-scales. We also see that both AVISO and NEMO isolines get flatter (stretched horizontally) as τ increases, such that at $\tau \approx 300$ days, there is almost equal energy at all scales between $\ell \approx 100$ km and $\ell \approx 1000$ km.

5 Conclusions

5.1 Summary of the main results

In this paper, we have exhibited a suite of analysis insights available from a coarse-graining approach that is relatively new in physical oceanography. As part of our coarse-grained analysis of numerical model and satellite analysis products, we found that the surface geostrophic kinetic energy is dominated by the mesoscale flow, thus supporting our understanding that it is the most energetic component of the general circulation (Ferrari & Wunsch, 2009). More precisely, our use of coarse-graining to measure the *global* spectrum (Sadek & Aluie, 2018), reveals that $\approx 60\%$ of the surface geostrophic kinetic energy resides at scales between 100 km and 500 km. We also found that the kinetic energy has a clear seasonality, peaking in the spring of both hemispheres, thus supporting analysis using different methods by Qiu et al. (2014) and Steinberg et al. (2021). Furthermore, results of the

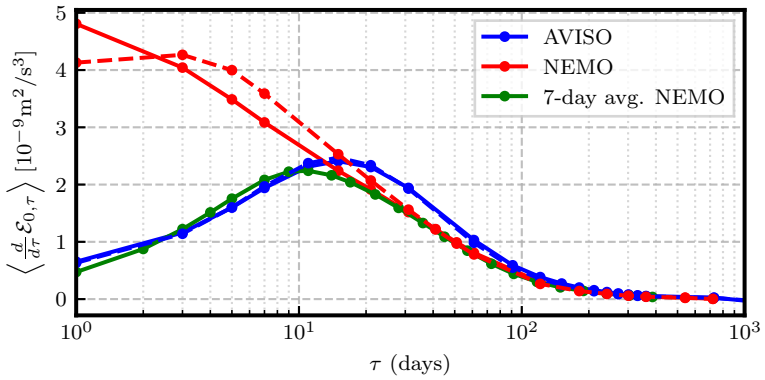

Figure 13. Evidence that the disagreement between AVISO and NEMO over time-scales $\lesssim$ 10 days is due to temporal averaging used in generating the gridded AVISO product. Here, we show temporal spectra from AVISO (blue) and NEMO (red) in the North (solid lines) and South (dashed lines), which disagree over $\tau \lesssim 10$ days as in Figure 12. However, the temporal spectra from NEMO agree with those from AVISO after applying a 7-day temporal smoothing to the original NEMO velocities (green). This result supports our hypothesis that AVISO is missing dynamical information at time-scales less than 10 days due to temporal smoothing over all length-scales.

global energy spectrum from both AVISO satellite analysis and NEMO model are consistent.

By coarse-graining in both space and time, we have shown that every length-scale evolves over a wide range of time-scales. This result makes temporal averaging, which is traditionally used to decompose oceanic flow into a mean and fluctuating components, unable to decompose the flow according to length-scales. Indeed, we showed that temporal averaging reduces the energy at all length-scales and not just the mesoscales. We found that the mean flow from a 9-year average has over 50% of its energy residing at length-scales smaller than 500 km. This result makes us appreciate the significance of temporally coherent forcing mechanisms acting on the mesoscales, such as bottom topography and continental boundaries.

An important contribution of this work is to demonstrate how a combined spatio-temporal coarse-graining analysis in Section 4.6 is able to expose hidden properties in the data. We did so by showing that the gridded AVISO product misrepresents the SSH-derived velocity over time-scales less than $\approx$ 10 days at *all length-scales*, including at $\approx$ 1000 km. The misrepresentation, however, was most severe over scales $\lesssim$ 500 km. We showed evidence supporting our hypothesis that this deficiency in AVISO is due to the temporal averaging (optimal interpolation) required for generating a gridded product from altimeter along-track measurements (Pujol et al., 2016). This deficiency is unravelled from a combined spatio-temporal analysis but not by a spatial scale analysis alone. In fact, AVISO has a spatial resolution (Ballarotta et al., 2019) comparable to that of the NEMO model we analyzed here and their spatial spectra agree well at all resolved spatial scales. We conjecture that the discrepancy between AVISO and NEMO is due to unbalanced motions in NEMO that is absent from AVISO, including at scales larger than 500 km.

5.2 Coarse-graining and the filtering spectrum

The coupling between different length- and time-scales and also between different geographic regions presents a major difficulty in understanding, modeling, and predicting oceanic circulation and mixing. Indeed, the oceanic kinetic energy budget is estimated to suffer from large uncertainties (Ferrari & Wunsch, 2009). A major reason behind these difficulties is a lack of scale-analysis methods that are appropriate in the *global* ocean.

In this paper, we have demonstrated the versatility of coarse-graining in serving as a robust scale-analysis method for the global ocean circulation that complements existing methods. The approach is very general, allows for probing the dynamics simultaneously in scale and in space, and is not restricted by assumptions of homogeneity or isotropy commonly required for traditional methods such as Fourier or structure-function analysis. Therefore, coarse-graining offers a way to probe and to quantify the energy budget at different length-scales globally while maintaining local information about the heterogeneous oceanic regions.

Here, we have also demonstrated how the recently developed *filtering spectrum* (Sadek & Aluie, 2018), which relies on coarse-graining, can be used to quantify the energy spectrum in the ocean. The method frees us from the limitations of Fourier boxes, and allows us to extract the spectrum globally. We view this work as a necessary step toward constructing a scale-aware global Lorenz Energy Cycle for the ocean circulation.

Appendix A Deforming the kernel around land

As outlined in section 2.1, filtering with a constant kernel while treating land as zero-velocity water and including land cells ("Fixed Kernel w/ Land") in the final tally is guaranteed to conserve 100% of the energy, while excluding land cells and integrating only over water cells ("Fixed Kernel w/o Land") leads to a loss of about 11% of the total kinetic energy at a filter scale of 2000 km (see Figure 2). This result follows since some of the kinetic energy 'smears' onto the land cells, which are then excluded from the spatial integrals.

An alternative approach is to deform the kernel around land ("Deforming Kernel") so that only water cells are incorporated in the filtering operation. This approach has the advantage of not needing to treat land as water, yet we have shown in Figure 2 that this choice still does not conserve 100% of the energy, sometimes even yielding larger values, albeit still within 1% error. Here, we explain why a deforming a kernel cannot be expected to yield 100% of the energy, unlike the "Fixed Kernel w/ Land."

To illustrate how the loss of energy conservation can happen with the Deforming Kernel method, consider a one-dimensional domain with five equally spaced points and a simple kernel that has a weight of 2 at the target point, 1 at neighbouring points, and 0 otherwise.

If the domain were periodic then the filtering operation could be represented as the matrix

$$G := \begin{bmatrix} 1/2 & 1/4 & 0 & 0 & 1/4 \\ 1/4 & 1/2 & 1/4 & 0 & 0 \\ 0 & 1/4 & 1/2 & 1/4 & 0 \\ 0 & 0 & 1/4 & 1/2 & 1/4 \\ 1/4 & 0 & 0 & 1/4 & 1/2 \end{bmatrix}$$

such that $\overline{\mathrm{KE}} = G \cdot \mathrm{KE}$, where KE is a column vector. Note that the sum of each row of G is 1, a result of normalizing the kernel (assuming a grid spacing of 1 for simplicity).

Domain integrating in this scenario is simply left-multiplying by the row vector $S := [1, 1, 1, 1, 1]$, which is equivalent to taking a column-wise sum. Since $S \cdot G = S$, $S \cdot \overline{\mathrm{KE}} = S \cdot G \cdot \mathrm{KE} = S \cdot \mathrm{KE}$, and so the domain integrated kinetic energy is conserved.

However, if the domain is non-periodic (such as if the edges were 'land'), then the resulting filtering kernel according to the Deformed Kernel approach that excludes anything outside the boundaries would be

$$G := \begin{bmatrix} 2/3 & 1/3 & 0 & 0 & 0 \\ 1/4 & 1/2 & 1/4 & 0 & 0 \\ 0 & 1/4 & 1/2 & 1/4 & 0 \\ 0 & 0 & 1/4 & 1/2 & 1/4 \\ 0 & 0 & 0 & 1/3 & 2/3 \end{bmatrix}$$

In this case, $S \cdot G = [11/12, 13/12, 1, 13/12, 11/13] \neq S$, and so in general $S \cdot \overline{\mathrm{KE}} \neq S \cdot \mathrm{KE}$. Moreover, there is no guarantee that $S \cdot \overline{\mathrm{KE}} \leq S \cdot \mathrm{KE}$, and so it may be that the total filtered kinetic energy exceeds the total unfiltered kinetic energy.

As observed, in general the error arising from deforming the kernel will be much smaller than that of treating land as zero-velocity water and only integrating over true water cells, especially for large filter kernels. However, again, it is worth recognizing that deforming the kernel does not guarantee energy conservation. To fully conserves energy and maintain commutativity with differentiation, we choose the "Fixed Kernel w/ Land" option, which treats land as zero-velocity water and include land cells in spatial integrals to compute total energy. Figure A1 shows the spectra obtained from implementing the three different coarse-graining possibilities.

Acknowledgments

We thank D. Balwada, M. Jansen, H. Khatri, and S. Rai for valuable discussions and comments. This research was funded by US NASA grant 80NSSC18K0772. HA was also supported by US DOE grants DE-SC0014318, DE-SC0020229, DE-SC0019329, NSF grant PHY-2020249, and US NNSA grants DE-NA0003856, DE-NA0003914. Computing time was provided by NERSC under Contract No. DE-AC02-05CH11231 and NASA's HEC Program through NCCS at Goddard Space Flight Center. This study has been conducted using E.U. Copernicus Marine Service Information. The product identifier of the AVISO dataset used in this work is "SEALEVEL_GLO_PHY_L4_REP_OBSERVATIONS_008_047", and can be downloaded at `https://marine.copernicus.eu/services-portfolio/access-to-products/`. The product identifier of the NEMO dataset is "GLOBAL_ANALYSISFORECAST_PHY_CPL_001_015", and is available at `https://marine.copernicus.eu/services-portfolio/access-to-products/`.

References

Aluie, H. (2013, March). Scale decomposition in compressible turbulence. *Physica D: Nonlinear Phenomena*, *247*(1), 54–65.

Aluie, H. (2017, January). Coarse-grained incompressible magnetohydrodynamics: analyzing the turbulent cascades. *New Journal of Physics*, *19*, 025008.

Aluie, H. (2019). Convolutions on the sphere: commutation with differential operators. *GEM-International Journal on Geomathematics*, *10*(1), 9.

Aluie, H., & Eyink, G. (2009, November). Localness of energy cascade in hydrodynamic turbulence. II. Sharp spectral filter. *Phys. Fluids*, *21*(11), 115108.

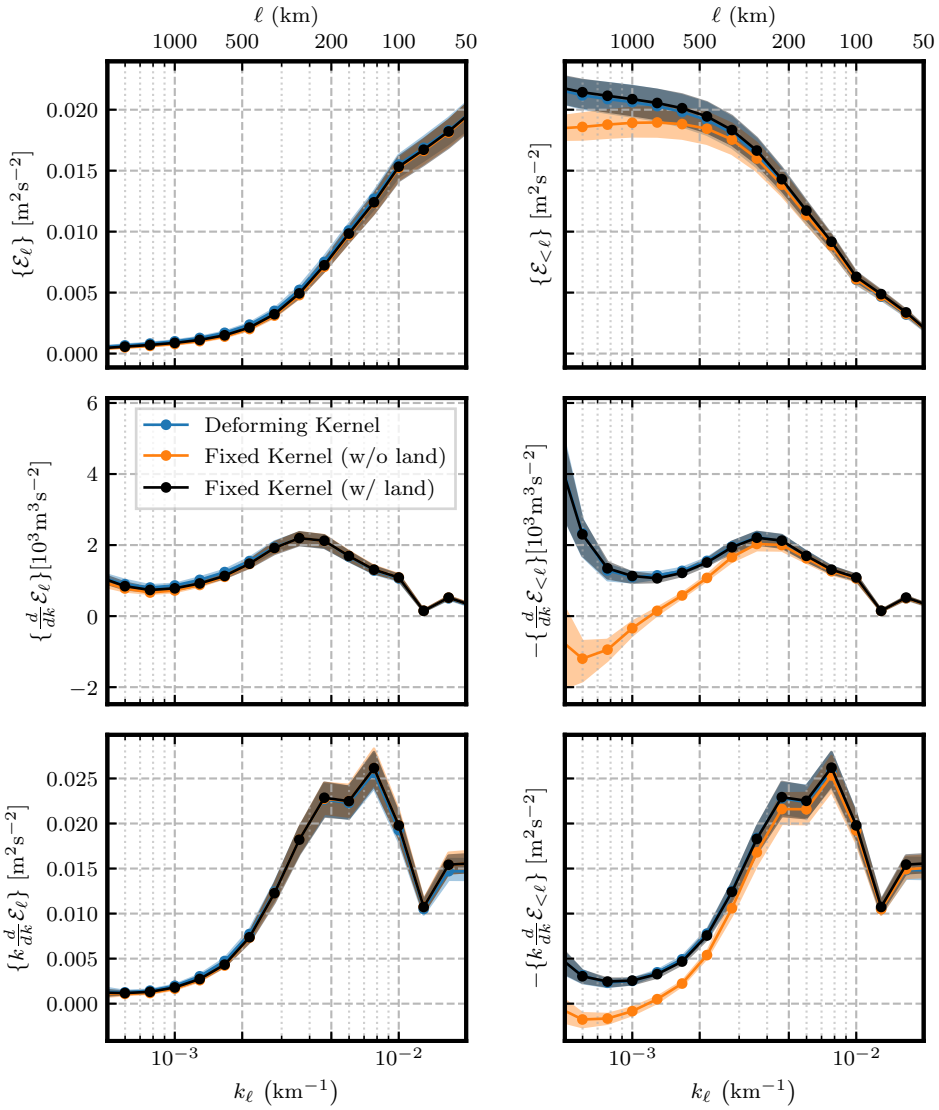

Figure A1. Comparison of three land treatment methods: deforming around land (blue), fixed kernel excluding land (orange), and fixed kernel including land (black). Vertical labels describe what is plotted in each panel. Left column corresponds to coarse KE and right column to fine KE. Top row presents cumulative KE spectra, middle row the k-derivative of the cumulative KE, and bottom row the $\log(k)$-derivative of cumulative KE. Note that the y-axis is common within each row. Data corresponds to North of the Tropics. Envelope shows inter-quartile range (25th to 75th percentiles) of temporal variation.

Aluie, H., Hecht, M., & Vallis, G. K. (2018). Mapping the energy cascade in the north atlantic ocean: The coarse-graining approach. *Journal of Physical Oceanography*, *48*(2), 225–244.

Aluie, H., Li, S., & Li, H. (2012, June). Conservative Cascade of Kinetic Energy in Compressible Turbulence. *Astrophys. J. Lett.*, *751*, L29.

Arbic, B. K., Müller, M., Richman, J. G., Shriver, J. F., Morten, A. J., Scott, R. B., ... Penduff, T. (2014). Geostrophic turbulence in the frequency–wavenumber domain: Eddy-driven low-frequency variability. *Journal of Physical Oceanography*, *44*(8), 2050–2069.

Arbic, B. K., Polzin, K. L., Scott, R. B., Richman, J. G., & Shriver, J. F. (2013, February). On Eddy Viscosity, Energy Cascades, and the Horizontal Resolution of Gridded Satellite Altimeter Products*. *Journal of Physical Oceanography*, *43*(2), 283–300.

Arbic, B. K., Scott, R. B., Flierl, G. R., Morten, A. J., Richman, J. G., & Shriver, J. F. (2012). Nonlinear cascades of surface oceanic geostrophic kinetic energy in the frequency domain. *Journal of Physical Oceanography*, *42*(9), 1577–1600.

Ballarotta, M., Ubelmann, C., Pujol, M.-I., Taburet, G., Fournier, F., Legeais, J.-F., ... others (2019). On the resolutions of ocean altimetry maps. *Ocean Science*, *15*(4), 1091–1109.

Barkan, R., Srinivasan, K., Yang, L., McWilliams, J. C., Gula, J., & Vic, C. (2021). Oceanic mesoscale eddy depletion catalyzed by internal waves. *TBD*, *submitted*. doi: 10.1002/essoar.10507068.1

Bryan, F. O., Gent, P. R., & Tomas, R. (2014, January). Can Southern Ocean Eddy Effects Be Parameterized in Climate Models? . *Journal of Climate*, *27*(1), 411–425.

Bühler, O., Callies, J., & Ferrari, R. (2014, October). Wave-vortex decomposition of one-dimensional ship-track data. *Journal of Fluid Mechanics*, *756*, 1007–1026.

Busecke, J. J. M., & Abernathey, R. P. (2019, January). Ocean mesoscale mixing linked to climate variability. *Science Advances*, *5*, eaav5014–.

Buzzicotti, M., Aluie, H., Biferale, L., & Linkmann, M. (2018). Energy transfer in turbulence under rotation. *Physical Review Fluids*, *3*(3), 034802.

Buzzicotti, M., Linkmann, M., Aluie, H., Biferale, L., Brasseur, J., & Meneveau, C. (2018). Effect of filter type on the statistics of energy transfer between resolved and subfilter scales from a-priori analysis of direct numerical simulations of isotropic turbulence. *Journal of Turbulence*, *19*(2), 167–197.

Callies, J., & Wu, W. (2019, September). Some Expectations for Submesoscale Sea Surface Height Variance Spectra. *Journal of Physical Oceanography*, *49*(9), 2271–2289.

Chen, R., Gille, S. T., McClean, J. L., Flierl, G. R., & Griesel, A. (2015, July). A Multiwavenumber Theory for Eddy Diffusivities and Its Application to the Southeast Pacific (DIMES) Region. *Journal of Physical Oceanography*, *45*(7), 1877–1896.

Eyink, G., & Aluie, H. (2009, November). Localness of energy cascade in hydrodynamic turbulence. I. Smooth coarse graining. *Phys. Fluids*, *21*(11), 115107.

Eyink, G. L. (1995). Local energy flux and the refined similarity hypothesis. *J. Stat. Phys.*, *78*, 335-351. doi: 10.1007/BF02183352

Eyink, G. L. (2005). Locality of turbulent cascades. *Physica D*, *207*, 91-116. doi: 10.1016/j.physd.2005.05.018

Ferrari, R., & Wunsch, C. (2009, January). Ocean Circulation Kinetic Energy: Reservoirs, Sources, and Sinks. *Annual Review of Fluid Mechanics*, *41*(1), 253–282.

Fox-Kemper, B., Danabasoglu, G., Ferrari, R., Griffies, S., Hallberg, R., Holland, M., ... Samuels, B. (2011). Parameterization of mixed layer eddies. iii: Implementation and impact in global ocean climate simulations. *Ocean Modelling*,

39(1-2), 61–78.

Fu, L.-L., & Smith, R. D. (1996, November). Global Ocean Circulation from Satellite Altimetry and High-Resolution Computer Simulation. *Bulletin of the American Meteorological Society*, *77*(1), 2625–2636.

Germano, M. (1992). Turbulence - The filtering approach. *J. Fluid Mech.*, *238*, 325-336. doi: 10.1017/S0022112092001733

Germano, M. (1992). Turbulence: the filtering approach. *Journal of Fluid Mechanics*, *238*, 325–336.

Griffies, S. M., Winton, M., Anderson, W. G., Benson, R., Delworth, T. L., Dufour, C. O., ... Zhang, R. (2015, February). Impacts on Ocean Heat from Transient Mesoscale Eddies in a Hierarchy of Climate Models. *Journal of Climate*, *28*(3), 952–977.

Grooms, I., Loose, N., Abernathey, R., Steinberg, J., Bachman, S., Marques, G., ... Yankovsky, E. (2021). Diffusion-based smoothers for spatial filtering of gridded geophysical data. *Journal of Advances in Modeling the Earth System*, *submitted*.

Haigh, M., Sun, L., Shevchenko, I., & Berloff, P. (2020). Tracer-based estimates of eddy-induced diffusivities. *Deep Sea Research Part I: Oceanographic Research Papers*, *160*, 103264.

Hewitt, H. T., Copsey, D., Culverwell, I. D., Harris, C. M., Hill, R. S. R., Keen, A. B., ... Hunke, E. C. (2011). Design and implementation of the infrastructure of hadgem3: the next-generation met office climate modelling system. *Geoscientific Model Development*, *4*(2), 223–253. Retrieved from `https://gmd.copernicus.org/articles/4/223/2011/` doi: 10.5194/gmd-4-223-2011

Jansen, M. F., Adcroft, A., Khani, S., & Kong, H. (2019). Toward an energetically consistent, resolution aware parameterization of ocean mesoscale eddies. *Journal of Advances in Modeling Earth Systems*, *11*(8), 2844–2860.

Kawabe, M. (1995). Variations of current path, velocity, and volume transport of the kuroshio in relation with the large meander. *Journal of physical oceanography*, *25*(12), 3103–3117.

Kelley, D. H., & Ouellette, N. T. (2011, November). Spatiotemporal persistence of spectral fluxes in two-dimensional weak turbulence. *Physics of Fluids*, *23*(1), 5101.

Kessler, W. S. (1990). Observations of long rossby waves in the northern tropical pacific. *Journal of Geophysical Research: Oceans*, *95*(C4), 5183–5217.

Khani, S., Jansen, M. F., & Adcroft, A. (2019). Diagnosing subgrid mesoscale eddy fluxes with and without topography. *Journal of Advances in Modeling Earth Systems*, *11*(12), 3995–4015.

Khatri, H., Sukhatme, J., Kumar, A., & Verma, M. K. (2018). Surface ocean enstrophy, kinetic energy fluxes, and spectra from satellite altimetry. *Journal of Geophysical Research: Oceans*, *123*(5), 3875–3892. doi: 10.1029/2017JC013516

Lea, D., Mirouze, I., Martin, M., King, R., Hines, A., Walters, D., & Thurlow, M. (2015). Assessing a new coupled data assimilation system based on the met office coupled atmosphere–land–ocean–sea ice model. *Monthly Weather Review*, *143*(11), 4678–4694.

Leonard, A. (1974). Energy Cascade in Large-Eddy Simulations of Turbulent Fluid Flows. *Adv. Geophys.*, *18*, A237.

Lieb, E. H., & Loss, M. (2001). Analysis 2nd eq. *American Mathematical Society, Providence, RI*, *14*, 348.

Linkmann, M., Buzzicotti, M., & Biferale, L. (2018). Multi-scale properties of large eddy simulations: correlations between resolved-scale velocity-field increments and subgrid-scale quantities. *Journal of Turbulence*, *19*(6), 493–527.

Martínez-Moreno, J., Hogg, A. M., England, M. H., Constantinou, N. C., Kiss, A. E., & Morrison, A. K. (2021). Global changes in oceanic mesoscale currents

over the satellite altimetry record. *Nature Climate Change*, 1–7.

Meneveau, C. (1994, February). Statistics of Turbulence Subgrid-Scale Stresses - Necessary Conditions and Experimental Tests. *Physics of Fluids*, *6*(2), 815–833.

Meneveau, C., & Katz, J. (2000). Scale-invariance and turbulence models for large-eddy simulation. *Annual Review of Fluid Mechanics*, *32*(1), 1–32.

O'Rourke, A. K., Arbic, B., & Griffies, S. (2018). Frequency-domain analysis of atmospherically forced versus intrinsic ocean surface kinetic energy variability in GFDL's CM2-O model hierarchy. *Journal of Climate*. doi: 10.1175/JCLI-D-17-0024.1

Pearson, B., Fox-Kemper, B., Bachman, S., & Bryan, F. (2017, July). Evaluation of scale-aware subgrid mesoscale eddy models in a global eddy-rich model. *Ocean Modelling*, *115*, 42–58.

Piomelli, U., Cabot, W. H., Moin, P., & Lee, S. (1991, July). Subgrid-scale backscatter in turbulent and transitional flows. *Physics of Fluids A (ISSN 0899-8213)*, *3*, 1766–1771.

Pope, S. B. (2001). *Turbulent flows*. IOP Publishing.

Pujol, M.-I., Faugère, Y., Taburet, G., Dupuy, S., Pelloquin, C., Ablain, M., & Picot, N. (2016). Duacs dt2014: the new multi-mission altimeter data set reprocessed over 20 years. *Ocean Sci*, *12*(5), 1067–1090.

Qiu, B., Chen, S., Klein, P., Sasaki, H., & Sasai, Y. (2014, December). Seasonal Mesoscale and Submesoscale Eddy Variability along the North Pacific Subtropical Countercurrent. *Journal of Physical Oceanography*, *44*, 3079–3098.

Qiu, B., Chen, S., Klein, P., Wang, J., Torres, H., Fu, L.-L., & Menemenlis, D. (2018, March). Seasonality in Transition Scale from Balanced to Unbalanced Motions in the World Ocean. *Journal of Physical Oceanography*, *48*, 591–605.

Rai, S., Hecht, M., Maltrud, M., & Aluie, H. (2021). Scale of oceanic eddy-killing by wind from global satellite observations. *Science Advances*. (under revision)

Richman, J. G., Arbic, B. K., Shriver, J. F., Metzger, E. J., & Wallcraft, A. J. (2012). Inferring dynamics from the wavenumber spectra of an eddying global ocean model with embedded tides. *Journal of Geophysical Research: Oceans*, *117*(C12).

Ringler, T., Petersen, M., Higdon, R. L., Jacobsen, D., Jones, P. W., & Maltrud, M. (2013, September). A multi-resolution approach to global ocean modeling. *Ocean Modelling*, *69*, 211–232.

Rivera, M. K., Aluie, H., & Ecke, R. E. (2014, May). The direct enstrophy cascade of two-dimensional soap film flows. *Physics of Fluids*, *26*(5).

Rocha, C. B., Chereskin, T. K., Gille, S. T., & Menemenlis, D. (2016, February). Mesoscale to Submesoscale Wavenumber Spectra in Drake Passage. *Journal of Physical Oceanography*, *46*, 601–620.

Sadek, M., & Aluie, H. (2018). Extracting the spectrum of a flow by spatial filtering. *Physical Review Fluids*, *3*(12), 124610.

Savage, A. C., Arbic, B. K., Alford, M. H., Ansong, J. K., Farrar, J. T., Menemenlis, D., ... Zamudio, L. (2017, October). Spectral decomposition of internal gravity wave sea surface height in global models. *Journal of Geophysical Research-Oceans*, *122*(1), 7803–7821.

Schubert, R., Gula, J., Greatbatch, R. J., Baschek, B., & Biastoch, A. (2020). The submesoscale kinetic energy cascade: Mesoscale absorption of submesoscale mixed layer eddies and frontal downscale fluxes. *Journal of Physical Oceanography*, *50*(9), 2573–2589.

Scott, R. B., & Arbic, B. K. (2007, March). Spectral Energy Fluxes in Geostrophic Turbulence: Implications for Ocean Energetics. *Journal of Physical Oceanography*, *37*(3), 673–688.

Scott, R. B., & Wang, F. (2005). Direct Evidence of an Oceanic Inverse Kinetic Energy Cascade from Satellite Altimetry. *Journal of Physical Oceanography*, *35*,

1650.

Sogge, C. D. (2008). *Fourier Integrals in Classical Analysis.* Cambridge University Press, New York.

Srinivasan, K., McWilliams, J. C., Molemaker, M. J., & Barkan, R. (2019). Submesoscale vortical wakes in the lee of topography. *Journal of Physical Oceanography*, *49*(7), 1949–1971.

Stanley, Z., Bachman, S., & Grooms, I. (2020). Vertical structure of ocean mesoscale eddies with implications for parameterizations of tracer transport. *Journal of Advances in Modeling Earth Systems*, *12*(10), e2020MS002151.

Stein, E. M., & Weiss, G. (1971). *Introduction to Fourier Analysis on Euclidean Spaces.* Princeton University Press, Princeton, New Jersey.

Steinberg, J., Cole, S. T., Drushka, K., & Abernathey, R. P. (2021). Observational evidence of the mesoscale inverse cascade in the global ocean. *TBD*, *submitted*.

Teeraratkul, C., & Aluie, H. (2021). Theory of large eddy simulation on the sphere. , *in preparation*.

Torres, H. S., Klein, P., Menemenlis, D., Qiu, B., Su, Z., Wang, J., ... Fu, L.-L. (2018, November). Partitioning Ocean Motions Into Balanced Motions and Internal Gravity Waves: A Modeling Study in Anticipation of Future Space Missions. *Journal of Geophysical Research-Oceans*, *123*(11), 8084–8105.

Vallis, G. K. (2017). *Atmospheric and Oceanic Fluid Dynamics.* Cambridge University Press. (2nd edition)

Vreman, B., Geurts, B., & Kuerten, H. (1994). Realizability conditions for the turbulent stress tensor in large-eddy simulation. *Journal of Fluid Mechanics*, *278*, 351–362.

Wunsch, C. (2007). The past and future ocean circulation from a contemporary perspective. *Geophysical Monograph-American Geophysical Union*, *173*, 53.

Youngs, M. K., Thompson, A. F., Lazar, A., & Richards, K. J. (2017, June). ACC Meanders, Energy Transfer, and Mixed Barotropic–Baroclinic Instability. *Journal of Physical Oceanography*, *47*(6), 1291–1305.

Zanna, L., Porta Mana, P., Anstey, J., David, T., & Bolton, T. (2017, March). Scale-aware deterministic and stochastic parametrizations of eddy-mean flow interaction. *Ocean Modelling*, *111*, 66–80.

Zhao, D., & Aluie, H. (2018, May). Inviscid criterion for decomposing scales . *Physical Review Fluids*, *3*(5), 301.

Figure 1.

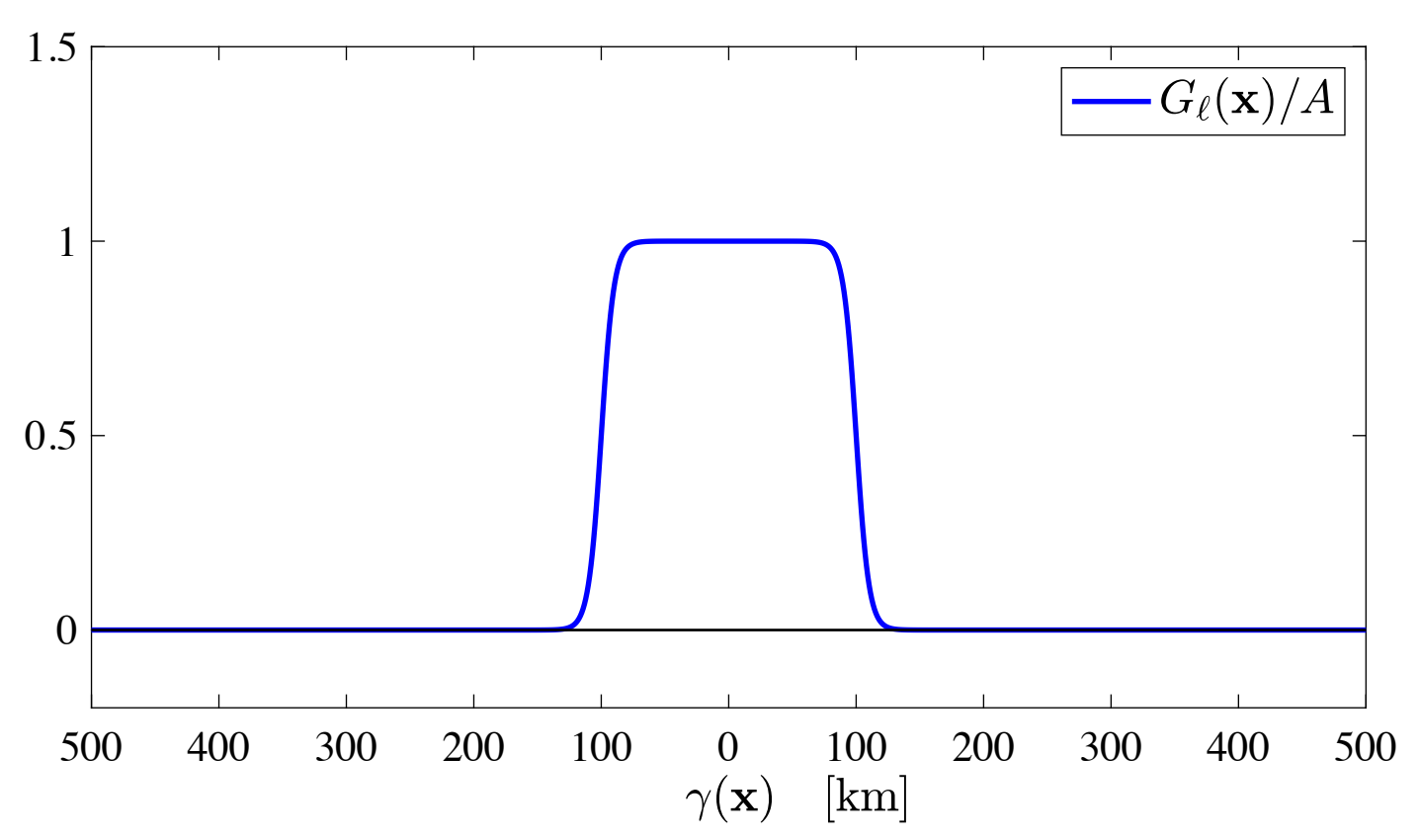
1.5
1
0.5
0
500
400
300
200
100
0
100
200
300
400
500
$\gamma(\mathbf{x})$ [km]
$G_\ell(\mathbf{x})/A$

Figure 2.

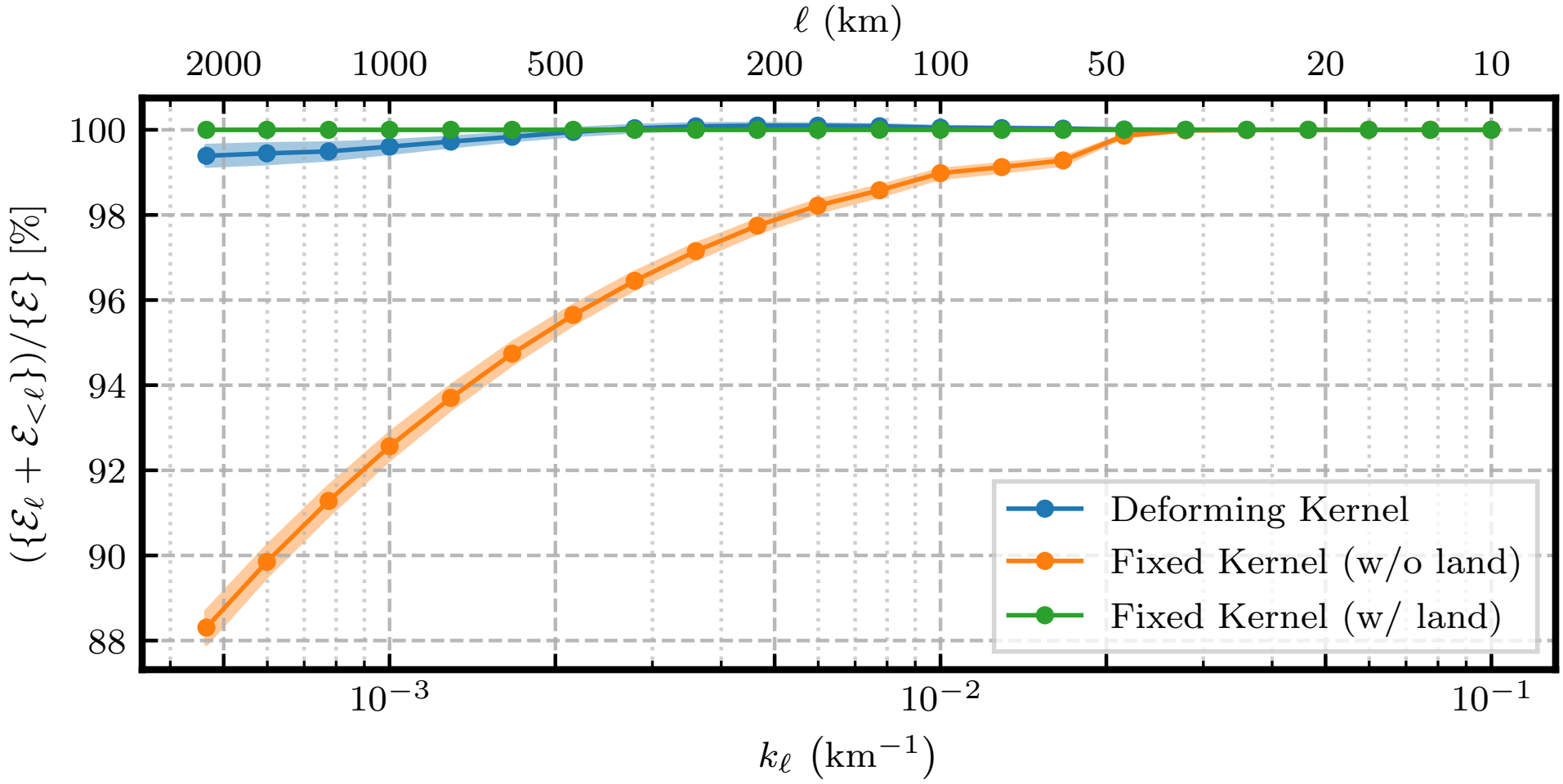
ℓ (km)
2000
1000
500
200
100
50
20
10
100
98
96
94
92
90
88
$(\{\varepsilon_\ell + \varepsilon_{<\ell}\})/\{\varepsilon\}$ [%]
10^{-3}
10^{-2}
10^{-1}
k_ℓ (km^{-1})
Deforming Kernel
Fixed Kernel (w/o land)
Fixed Kernel (w/ land)

Figure 3.

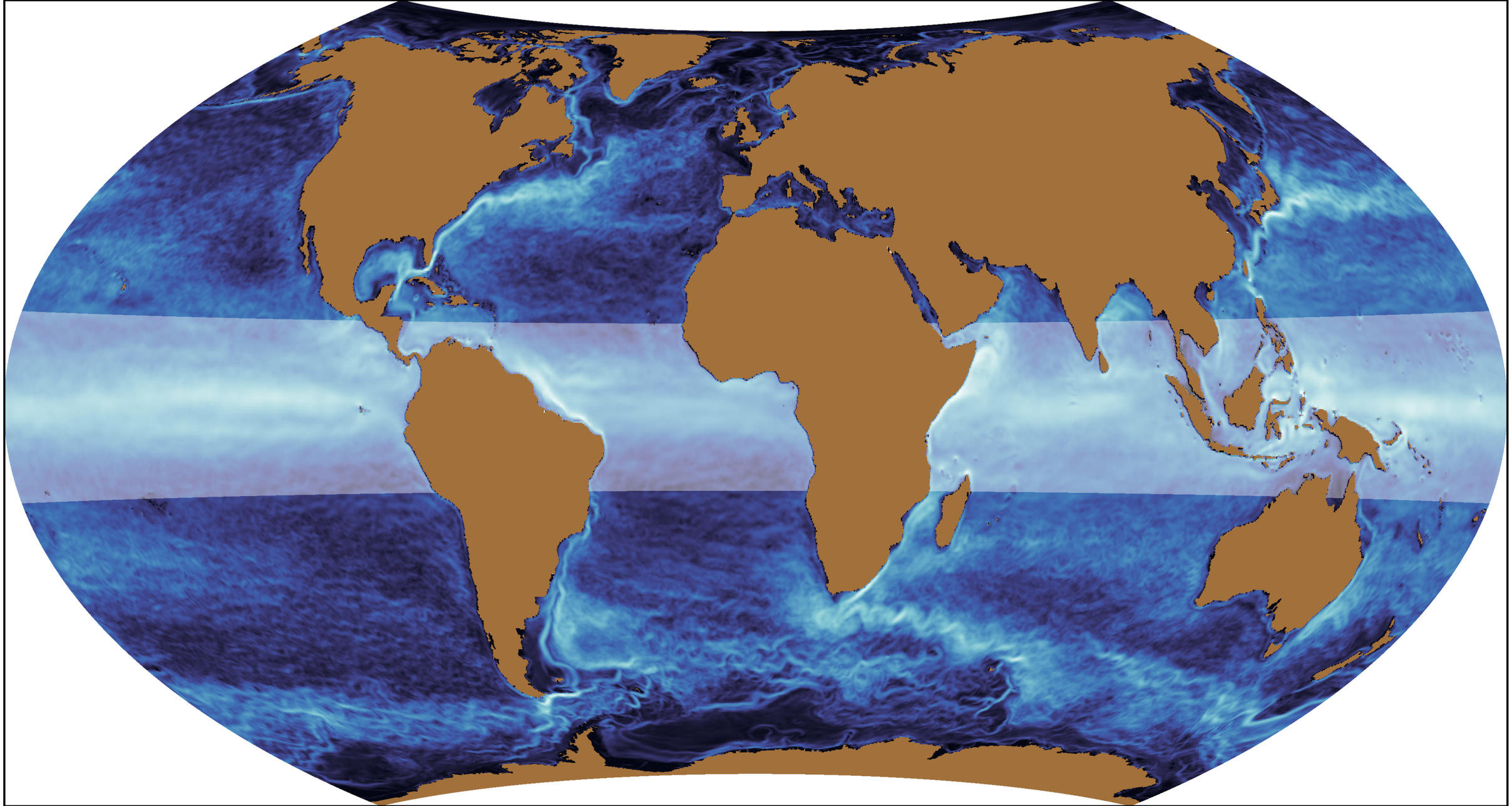

Figure 4.

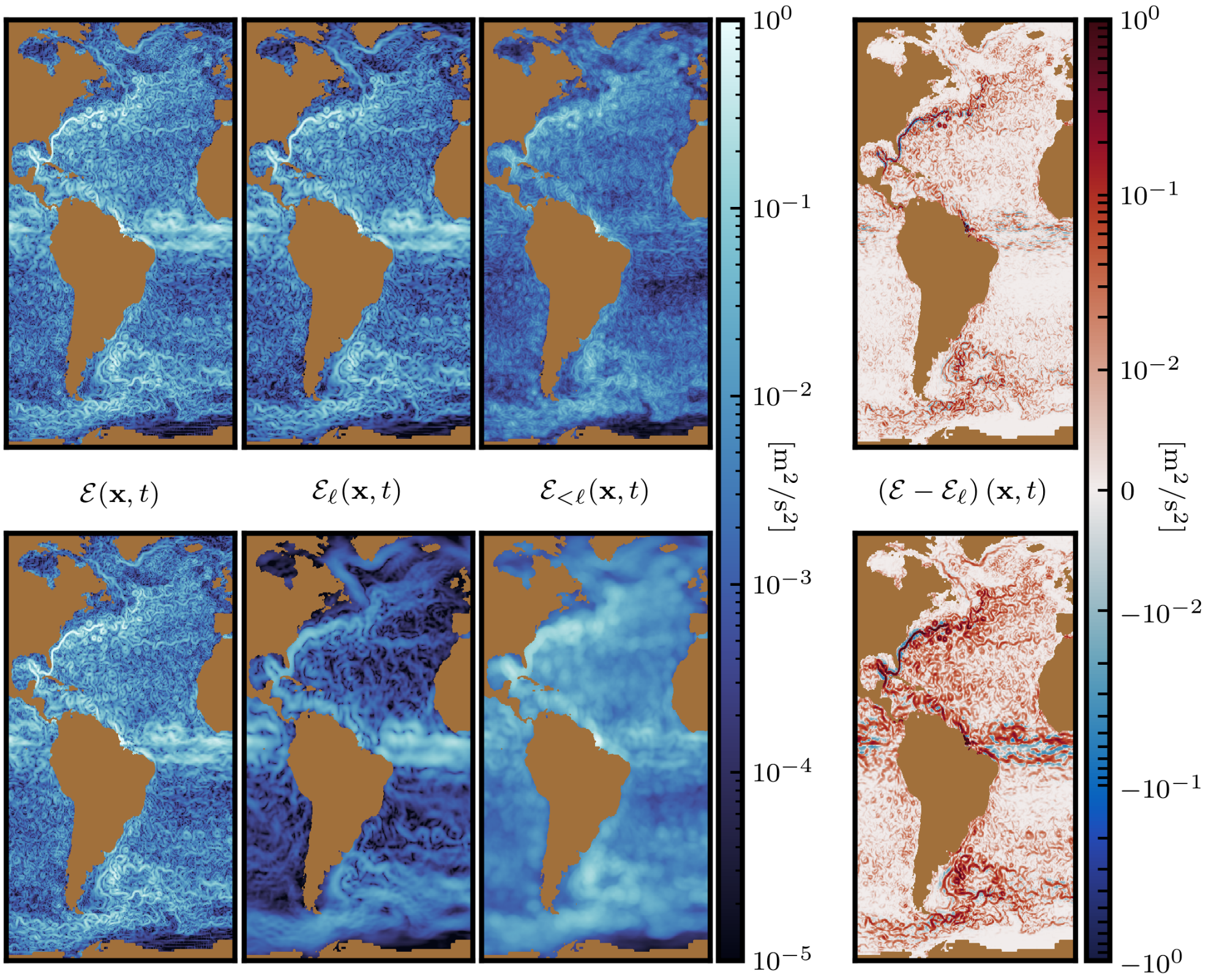
$\mathcal{E}(\mathbf{x},t)$
$\mathcal{E}_\ell(\mathbf{x},t)$
$\mathcal{E}_{<\ell}(\mathbf{x},t)$
$(\mathcal{E}-\mathcal{E}_\ell)(\mathbf{x},t)$
10^0
10^{-1}
10^{-2}
10^{-3}
10^{-4}
10^{-5}
$[\mathrm{m}^2/\mathrm{s}^2]$
10^0
10^{-1}
10^{-2}
0
-10^{-2}
-10^{-1}
-10^0
$[\mathrm{m}^2/\mathrm{s}^2]$

Figure 5.

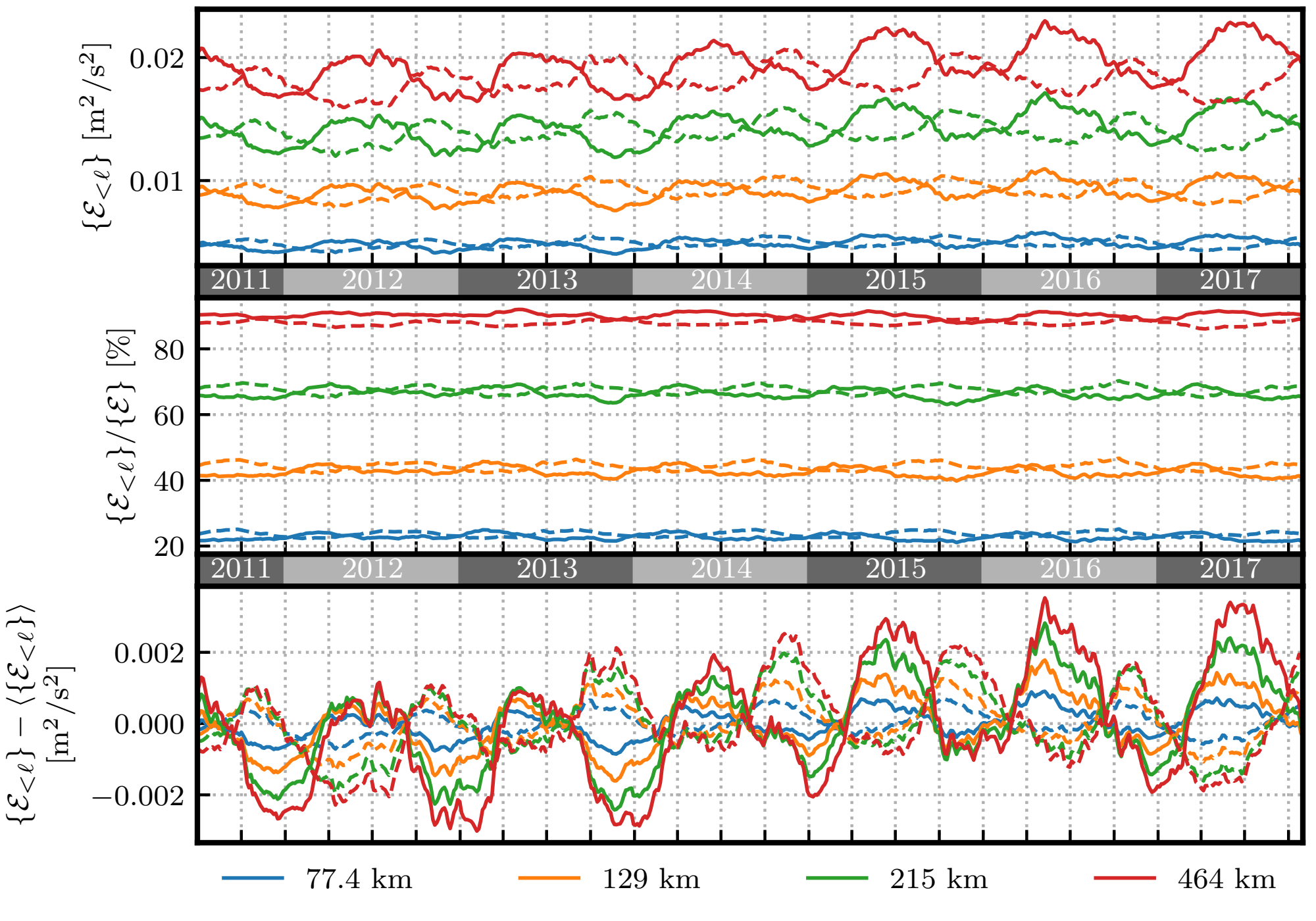
$\{\mathcal{E}_{<\ell}\}$ [m^2/s^2]
0.02
0.01
2011
2012
2013
2014
2015
2016
2017
$\{\mathcal{E}_{<\ell}\}/\{\mathcal{E}\}$ [%]
80
60
40
20
2011
2012
2013
2014
2015
2016
2017
$\{\mathcal{E}_{<\ell}\} - \langle\{\mathcal{E}_{<\ell}\}\rangle$ [m^2/s^2]
0.002
0.000
−0.002
77.4 km
129 km
215 km
464 km

Figure 6.

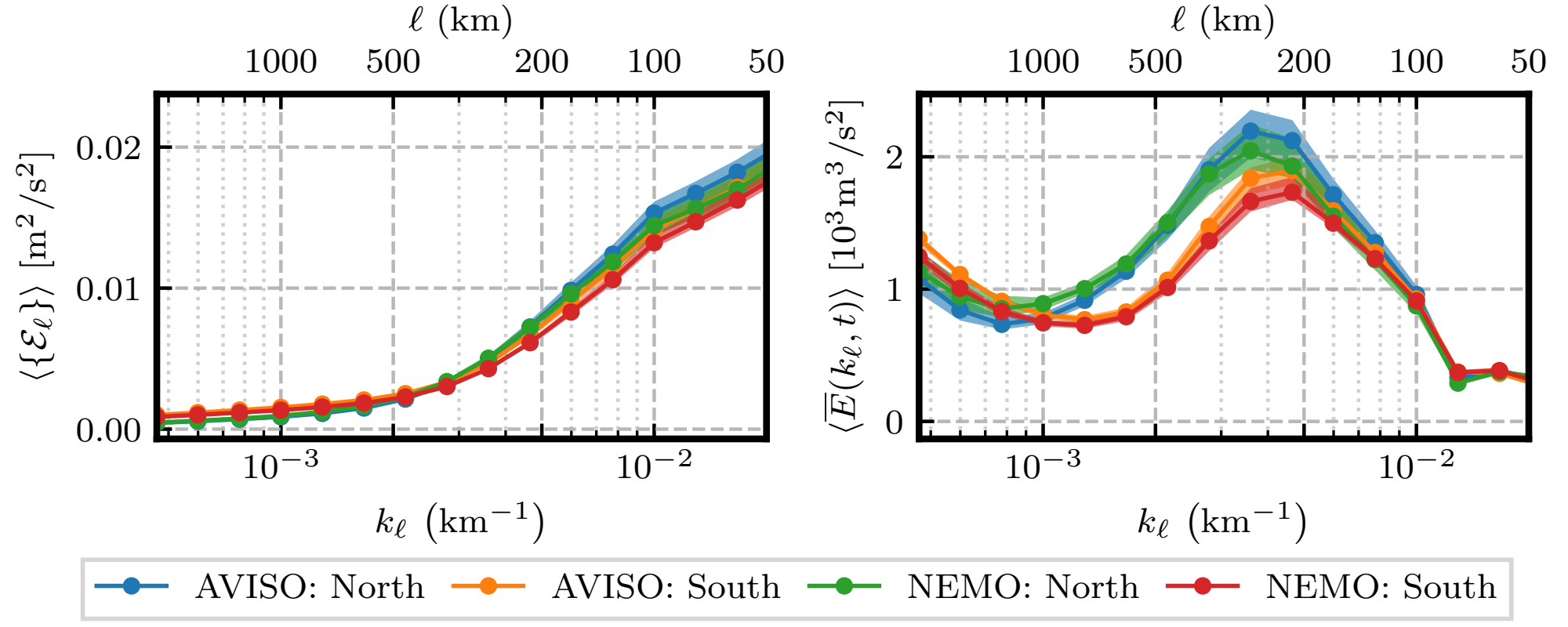
ℓ (km)
1000
500
200
100
50
0.02
0.01
0.00
$\langle\{\mathcal{E}_\ell\}\rangle$ [m^2/s^2]
10^{-3}
10^{-2}
k_ℓ (km^{-1})
ℓ (km)
1000
500
200
100
50
2
1
0
$\langle\overline{E}(k_\ell,t)\rangle$ [10^3m^3/s^2]
10^{-3}
10^{-2}
k_ℓ (km^{-1})
AVISO: North
AVISO: South
NEMO: North
NEMO: South

Figure 7.

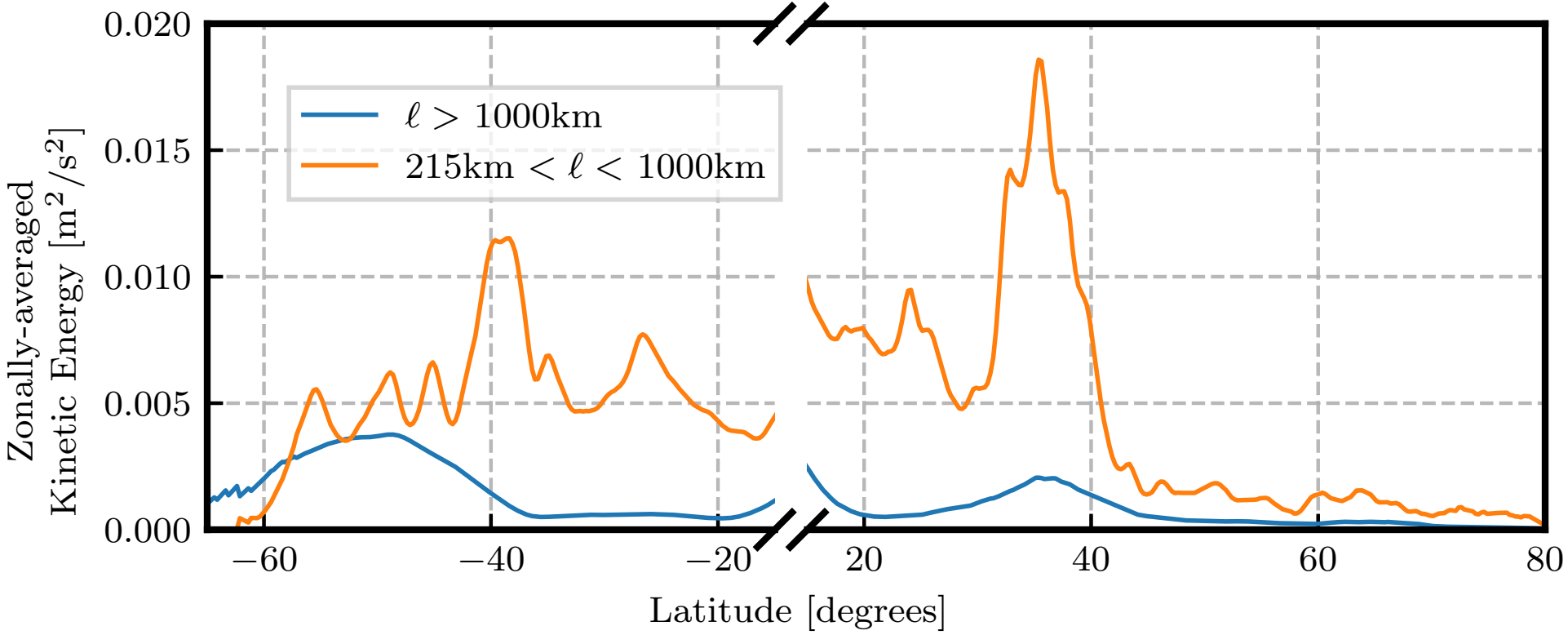
0.020
0.015
0.010
0.005
0.000
Zonally-averaged
Kinetic Energy [m^2/s^2]
$\ell > 1000$km
215km $< \ell <$ 1000km
−60
−40
−20
20
40
60
80
Latitude [degrees]

Figure 8.

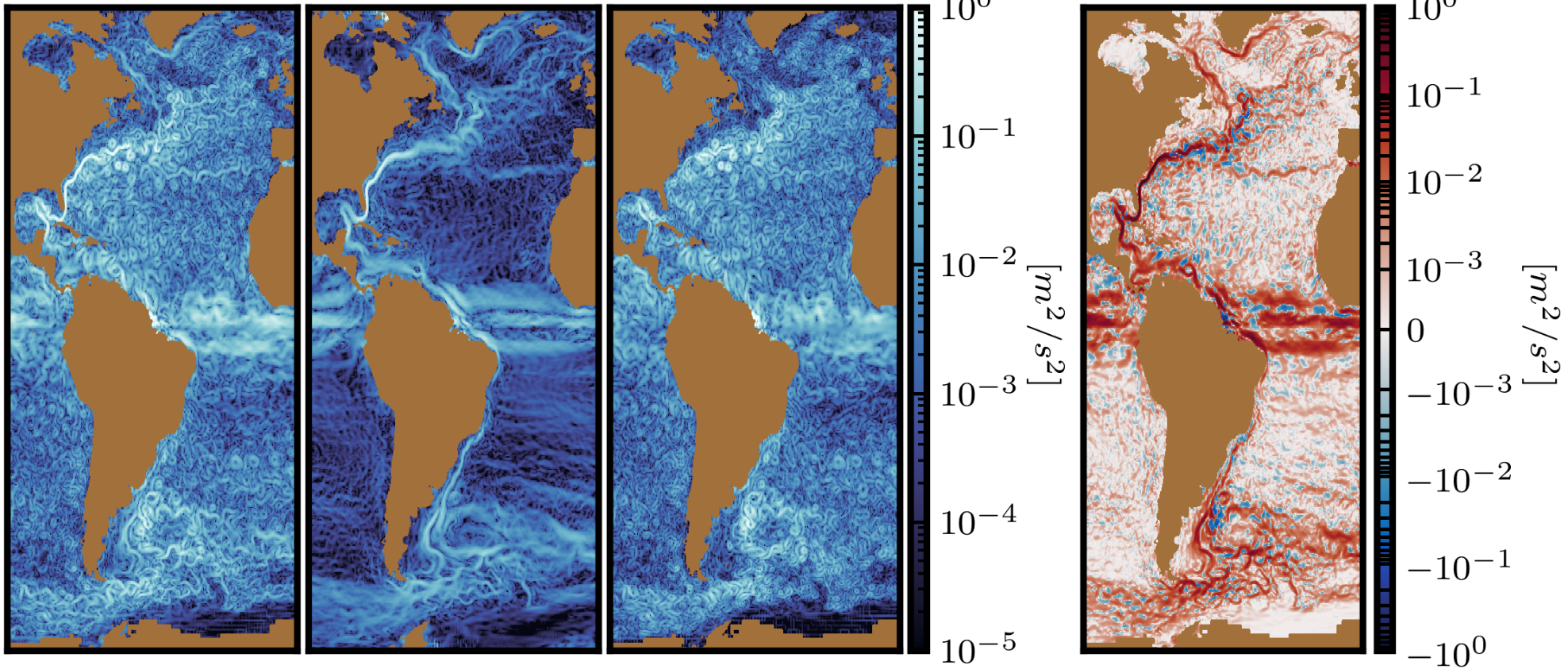

$\mathcal{E}(\mathbf{x},t)$ $MKE(\mathbf{x})$ $EKE(\mathbf{x},t)$ $\frac{1}{2}\left(\mathbf{u}' \cdot \langle \mathbf{u} \rangle\right)(\mathbf{x},t)$

Figure 9.

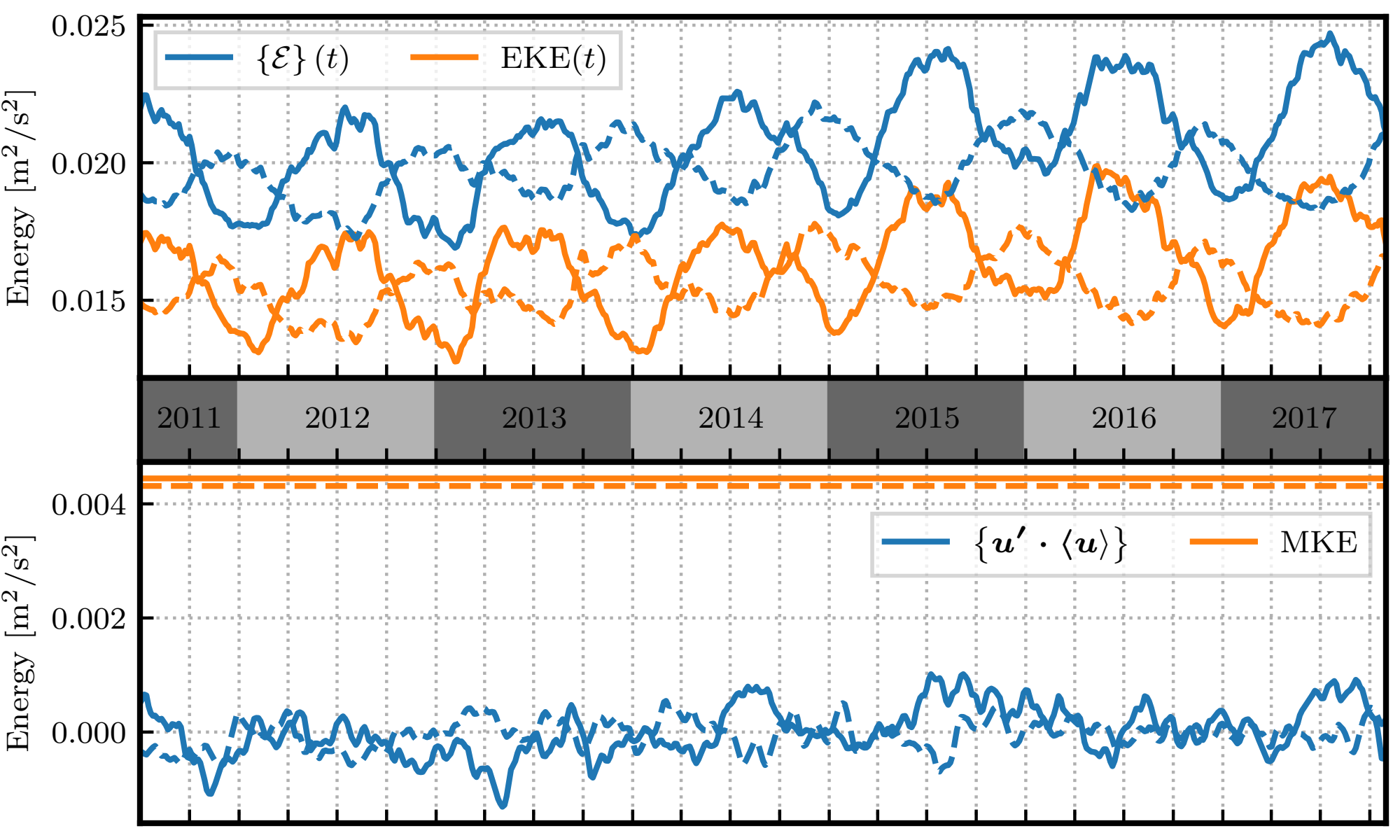
0.025
0.020
0.015
Energy [m^2/s^2]
$\{\mathcal{E}\}\,(t)$
EKE(t)
2011
2012
2013
2014
2015
2016
2017
0.004
0.002
0.000
Energy [m^2/s^2]
$\{\boldsymbol{u}' \cdot \langle \boldsymbol{u} \rangle\}$
MKE

Figure 10.

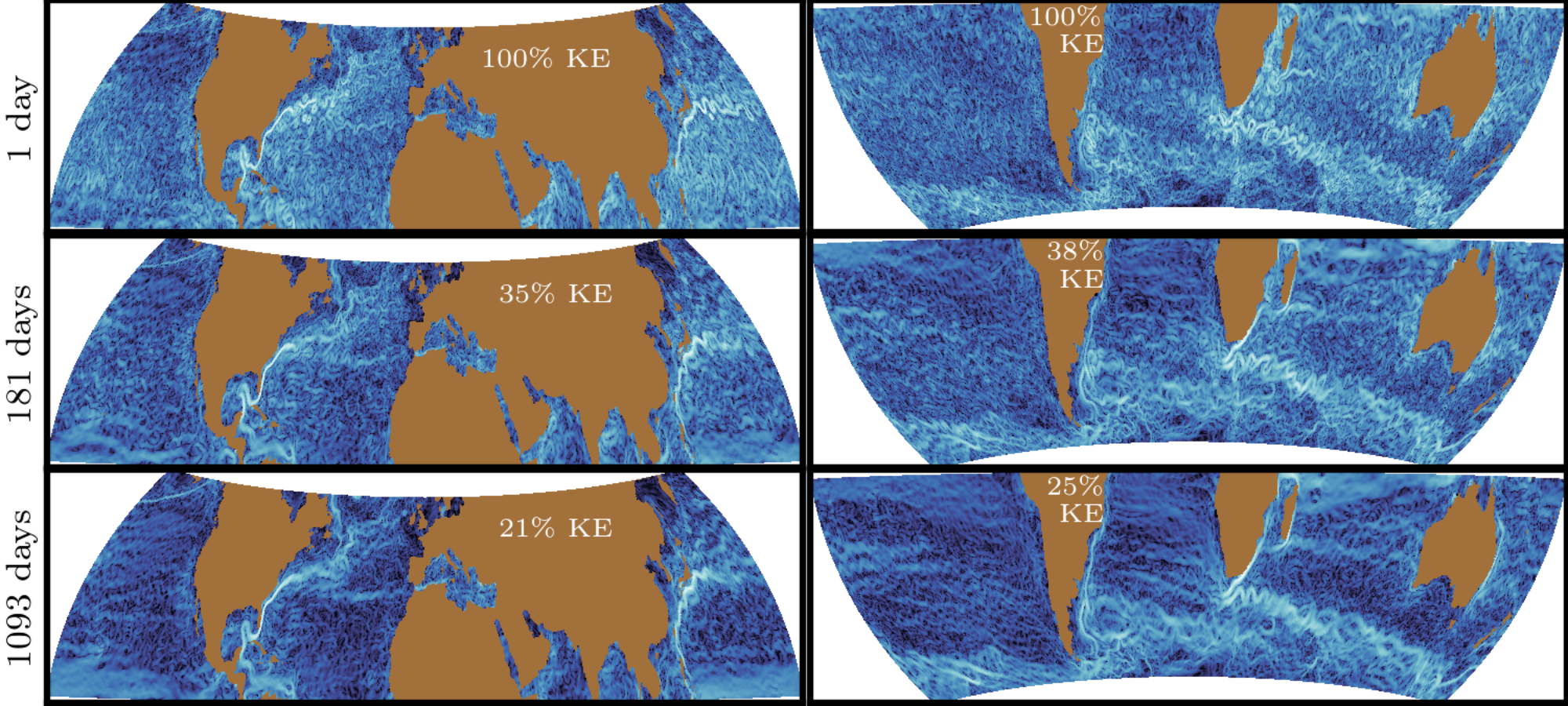
1 day
181 days
1093 days
100% KE
35% KE
21% KE
100%
KE
38%
KE
25%
KE

Figure 11.

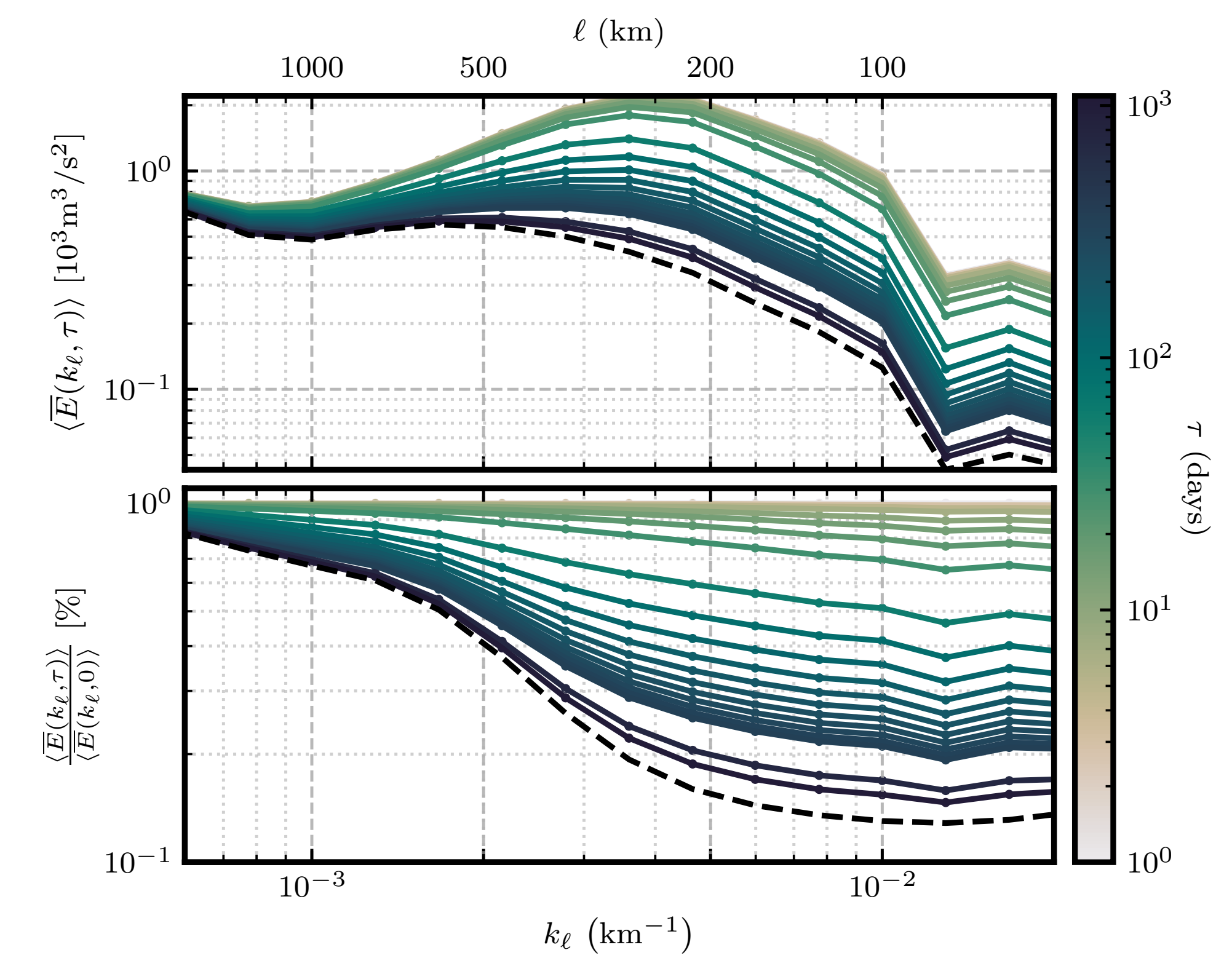
ℓ (km)
1000
500
200
100
10^0
10^{-1}
$\langle \overline{E}(k_\ell, \tau) \rangle$ $[10^3 \mathrm{m}^3/\mathrm{s}^2]$
10^0
10^{-1}
$\frac{\langle \overline{E}(k_\ell,\tau) \rangle}{\langle \overline{E}(k_\ell,0) \rangle}$ [%]
10^{-3}
10^{-2}
k_ℓ (km^{-1})
10^3
10^2
10^1
10^0
τ (days)

Figure 12.

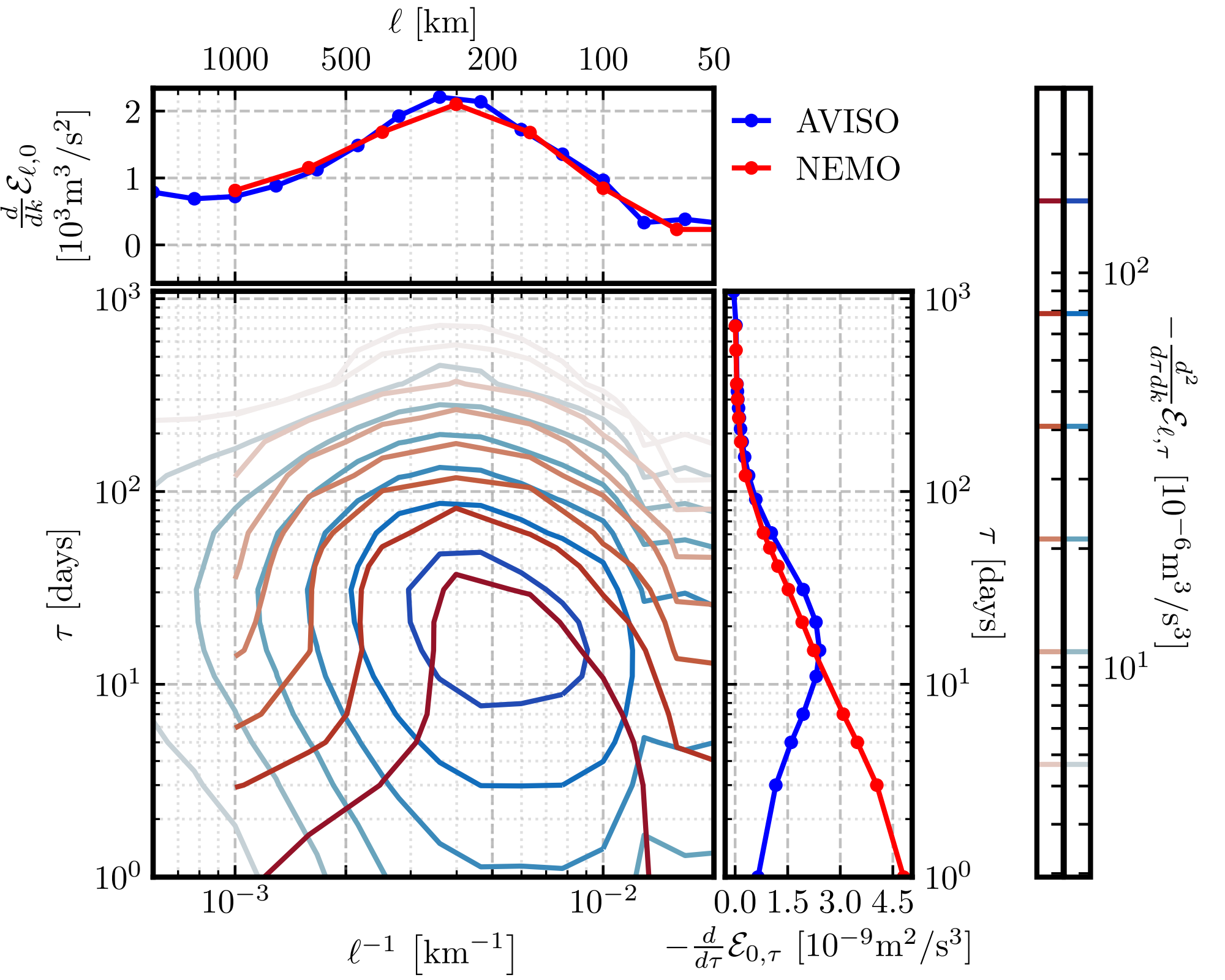
ℓ [km]
1000
500
200
100
50
$\frac{d}{dk}\mathcal{E}_{\ell,0}$ $[10^3\mathrm{m}^3/\mathrm{s}^2]$
2
1
0
AVISO
NEMO
10^3
10^2
10^1
10^0
τ [days]
10^{-3}
10^{-2}
ℓ^{-1} $[\mathrm{km}^{-1}]$
0.0
1.5
3.0
4.5
$-\frac{d}{d\tau}\mathcal{E}_{0,\tau}$ $[10^{-9}\mathrm{m}^2/\mathrm{s}^3]$
$-\frac{d^2}{d\tau dk}\mathcal{E}_{\ell,\tau}$ $[10^{-6}\mathrm{m}^3/\mathrm{s}^3]$

Figure 13.

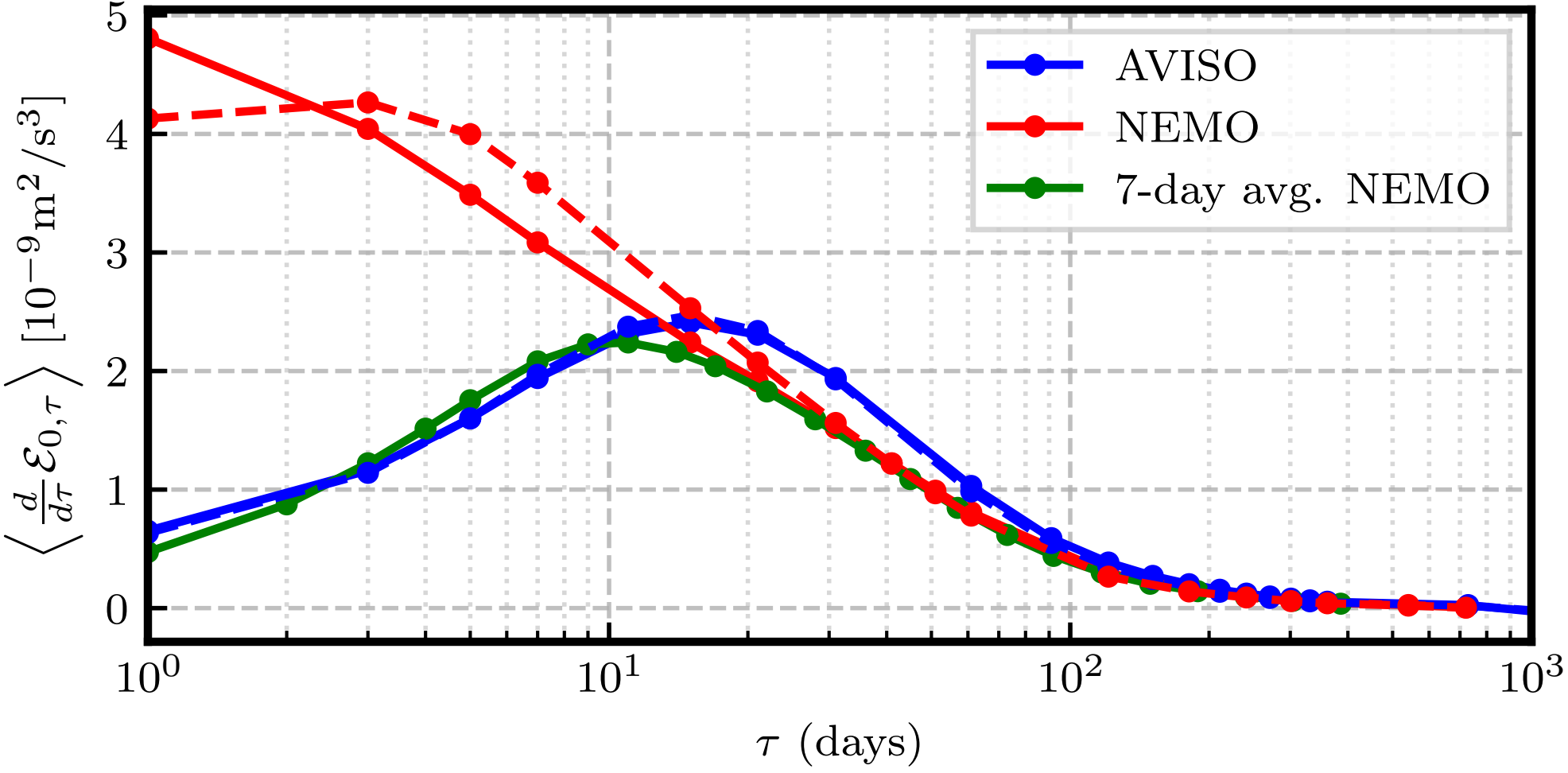
AVISO
NEMO
7-day avg. NEMO
$\left\langle \frac{d}{d\tau}\mathcal{E}_{0,\tau} \right\rangle$ [10^{-9}m^2/s^3]
τ (days)
0
1
2
3
4
5
10^0
10^1
10^2
10^3

Figure 14.

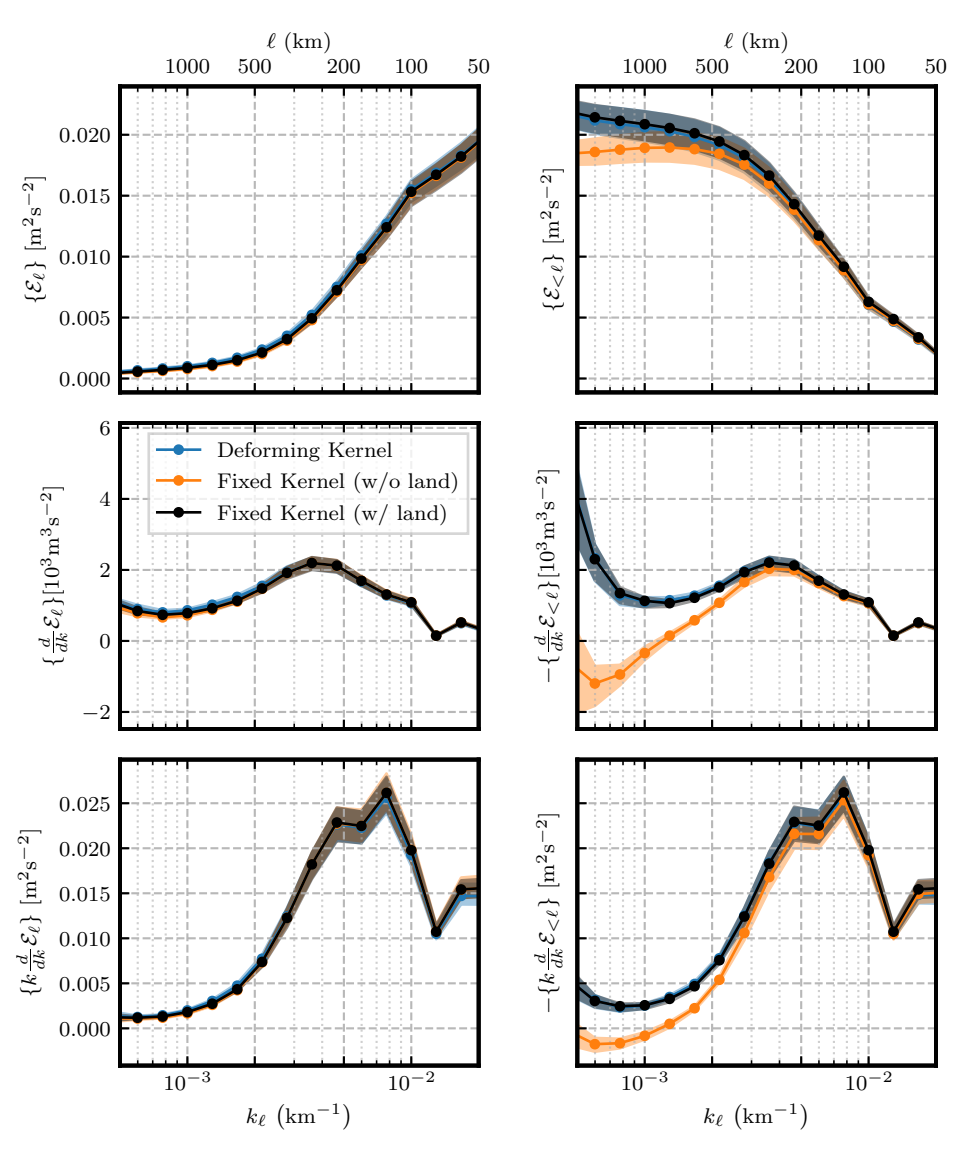
ℓ (km)
1000
500
200
100
50
$\{\mathcal{E}_\ell\}$ [m^{2}s^{-2}]
$\{\mathcal{E}_{<\ell}\}$ [m^{2}s^{-2}]
0.020
0.015
0.010
0.005
0.000
Deforming Kernel
Fixed Kernel (w/o land)
Fixed Kernel (w/ land)
$\{\frac{d}{dk}\mathcal{E}_\ell\}$[10^{3}m^{3}s^{-2}]
$-\{\frac{d}{dk}\mathcal{E}_{<\ell}\}$[10^{3}m^{3}s^{-2}]
6
4
2
0
−2
$\{k\frac{d}{dk}\mathcal{E}_\ell\}$ [m^{2}s^{-2}]
$-\{k\frac{d}{dk}\mathcal{E}_{<\ell}\}$ [m^{2}s^{-2}]
0.025
0.020
0.015
0.010
0.005
0.000
10^{-3}
10^{-2}
k_ℓ (km^{-1})